Research Square

Preprints are preliminary reports that have not undergone peer review.
They should not be considered conclusive, used to inform clinical practice,
or referenced by the media as validated information.

# Date palm waste-derived ozonized and nutrient doped biochar and carbon dots for heavy metals removal from multi-metal contaminated water

**Muhammad Usama**
King Saud University
**Munir Ahmad**
amunir@ksu.edu.sa
King Saud University
**Mohammad I. Al-Wabel**
King Saud University
**Jahangir Ahmad**
King Saud University
**Muhammad Imran Rafique**
King Saud University
**Hamed A. Al-Swadi**
King Saud University
**Abdullah S.F. Al-Farraj**
King Saud University

**Research Article**

**Keywords:** Slow pyrolysis, post-pyrolysis surface functionalization, heavy metal chemisorption, Langmuir isotherm, competitive sorption

**Posted Date:** November 20th, 2026

**DOI:** https://doi.org/10.21203/rs.3.rs-11103359/v1

**License:** This work is licensed under a Creative Commons Attribution 4.0 International License.
Read Full License

**Additional Declarations:** No competing interests reported.

# Date palm waste-derived ozonized and nutrient doped biochar and carbon dots for heavy metals removal from multi-metal contaminated water

Muhammad Usama, Munir Ahmad*, Mohammad I. Al-Wabel, Jahangir Ahmad, Muhammad Imran Rafique, Hamed A. Al-Swadi, Abdullah S.F. Al-Farraj

Soil Sciences Department, College of Food & Agricultural Sciences, King Saud University, P.O. Box 2460, Riyadh 11451, Kingdom of Saudi Arabia

*Corresponding author:
Munir Ahmad: amunir@ksu.edu.sa

*Present address:*
Muhammad Usama: Department of Ecosystem and Conservation Sciences, University of Montana, Missoula, Montana 59812, USA
Jahangir Ahmad: School of Earth, Atmosphere & Environment, Monash University, Clayton, Victoria 3800, Australia

## Abstract

Heavy metal (HM) contamination of surface water and groundwater from mining, industrial effluents and agrochemical sources is a persistent global problem. Converting agricultural waste into biochar offers a low-cost, circular route to overcome this problem; however, pyrolysis destroys much of the oxygen-bearing surface functionality on which HM binding depends. Post-pyrolysis oxidation or nutrient enrichment could restore this functionality. Therefore, date palm waste biochar (BC) pyrolyzed at 500°C was engineered through ozonization, nutrient doping with N, P and K and hydrothermal conversion into carbon dots (CD), alone and combined, yielding eight pyrolysis-derived materials characterized and tested for $Pb^{2+}$, $Cd^{2+}$, $Mn^{2+}$ and $Zn^{2+}$ removal from contaminated aqueous solution. Pyrolysis process increased the BET surface area from 4.30 to 52.32 $m^2\ g^{-1}$ (12-fold), yet ozonization and nutrient doping decreased it to by 35% to 72%, while restoring C–O–C, C–O and Si–O functionality and forming crystalline mineral phases. At pH 5 and 1 $g\ L^{-1}$, nutrient-doped ozonized carbon dots (NOCD) increased $Pb^{2+}$ removal from 43% to 97% and Langmuir capacity by 50% to 158% for all four competing metals, although $Pb^{2+}$ was retained preferentially ($Pb^{2+} > Zn^{2+} > Cd^{2+} > Mn^{2+}$). The uptake of HM increased with reducing surface area, indicating restored surface chemistry, not porosity, governed performance with pseudo-second-order kinetics and Dubinin–Radushkevich isotherm indicating monolayer chemisorption via complexation, cation exchange and surface precipitation. These results show that post-pyrolysis oxidative and nutrient functionalization can engineer pyrolysis into a scalable, low-cost sorbent for remediating multi-metal contaminated water.

**Keywords:** Slow pyrolysis; post-pyrolysis surface functionalization; heavy metal chemisorption; Langmuir isotherm; competitive sorption

## 1. Introduction

Heavy metal contamination of freshwater resources is among the most persistent environmental stressors confronting the world today. Rapid industrialization, mining, metal plating, battery manufacture and the discharge of untreated municipal effluent have loaded aquatic systems with $Pb^{2+}$, $Cd^{2+}$, $Mn^{2+}$ and $Zn^{2+}$ at concentrations that routinely exceed regulatory thresholds (Liu et al., 2017; Rahman and Singh, 2019). Unlike organic pollutants, these ions are non-biodegradable, persist indefinitely in the environment and accumulate progressively through the food chain (Liu et al., 2018). Chronic exposure to $Pb^{2+}$ and $Cd^{2+}$ is associated with neurological, renal and skeletal disorders and the World Health Organization has set drinking-water guideline values as low as 0.01 mg $L^{-1}$ for Pb and 0.003 mg $L^{-1}$ for Cd (World Health Organization, 2008). Even the comparatively less toxic $Mn^{2+}$ and $Zn^{2+}$ degrade water quality and disturb aquatic ecosystem function once their solubility limits are exceeded (Xu et al., 2019).

Conventional remediation technologies, including chemical precipitation, ion exchange, membrane filtration and electrochemical treatment, remove metals effectively but demand high capital and energy inputs, generate secondary sludge requiring disposal and lose efficiency at low residual concentrations typical of polished effluents (Liu et al., 2018; Xu et al., 2019). Adsorption remains the most operationally tractable alternative because it is simple to implement, reversible and effective across a wide concentration range (Babel and Kurniawan, 2003). However, its viability at the field scale depends largely on the cost and availability of the adsorbent, which has directed attention toward carbonaceous materials derived from agricultural residues rather than commercial activated carbon (Wang et al., 2023).

Date palm (*Phoenix dactylifera* L.) is one of the most widely cultivated and economically important perennial crops in arid and semi-arid regions, underpinning the agricultural economy of the Middle East and North Africa (Burezq and Davidson, 2023). Annual pruning generates large volumes of leaf and frond residue that is typically burned or landfilled, representing both a disposal burden and an underexploited carbon resource, so redirecting it toward engineered water-treatment sorbents addresses water, solid-waste and air-pollution objectives together. The chemistry of this residue makes it a particularly suitable sorbent precursor: its lignocellulosic matrix is rich in cellulose, hemicellulose and lignin, whose hydroxyl, carboxyl and phenolic groups are progressively dehydrated, decarboxylated and aromatized during pyrolysis. This thermal rearrangement collapses the fibrous cell wall into a porous aromatic carbon skeleton while retaining a residual population of oxygen-bearing edge groups that act as metal-binding sites and it concentrates the inherent mineral fraction into phases capable of surface precipitation and ion exchange (Gale et al., 2021; Xie et al., 2021).

Biochar produced from date palm residues has been evaluated for aqueous metal removal, with date seed-derived material reported to bind $Pb^{2+}$ effectively in both batch and column configurations (Mahdi et al., 2018) and two-step pyrolysis of date palm waste shown to improve Cu(II) uptake from wastewater (Mahmoud et al., 2024). Parallel work has established that the sorption performance of pristine biochar can be substantially increased by post-synthesis modification. Oxygenation by ozonization introduces carboxylic functionality and elevates cation exchange capacity by an order of magnitude (Valdés et al., 2002; Huff et al., 2018; Eldeeb et al., 2024), heteroatom doping with N and P enhances surface reactivity and binding-site density (Yuan et al., 2022; Ahmad et al., 2023) and carbon dots synthesized from the same date palm feedstock have demonstrated strong pollutant scavenging when composited with biochar (Ahmad et al., 2020; Chen et al., 2022).

Three limitations nevertheless constrain the translation of these findings. First, most reported systems have been tested against a single metal ion, whereas real effluents present competing cations whose relative affinities govern actual removal (Silos-Llamas et al., 2020; Wang et al., 2022). Second, ozonization and nutrient doping have been applied in isolation; thus, it remains unknown whether their effects on surface chemistry are additive, redundant, or antagonistic when imposed sequentially on the same carbon skeleton. Third, both treatments are reported to enrich surface functionality; however, each also deposits material within the pore network; the resulting trade-off between gained binding sites and lost accessible surface area has not been resolved for a biochar-carbon dot composite (Shaban et al., 2025; Zhang et al., 2025). Because the surface area and functional group density respond in opposite directions to these treatments, their combined effect cannot be predicted from the single-treatment literature and must be determined experimentally on a common feedstock under identical, competitive multi-metal sorption conditions.

To the best of our knowledge, there have been no studies investigating ozonization and nutrient doping (separately or together) on a shared biochar- carbon dots series derived date palm waste. Therefore, it was hypothesized that the combined application of engineered biochar and carbon-dot will enhance the chemisorptive capacity for $Pb^{2+}$, $Cd^{2+}$, $Mn^{2+}$ and $Zn^{2+}$ when these metals compete in a multi-metal solution, as the pyrolysis and post-pyrolysis oxidative or nutrient-based functionalization could potentially alter biochar and carbon-dot surface chemistry through distinct and non-additive mechanisms. In order to mimic the actual effluents that contains metals competing for the same binding sites, all sorption experiments were conducted with a mixed-metal solution that contains the four metals together in one batch so that removal, capacity and selectivity could be determined when they were competing to be sorbed. The significance of this study is twofold: it establishes how sequential post-pyrolysis treatments can be combined to engineer the surface chemistry of a regionally abundant pyrolysis feedstock, and it clarifies which surface property governs competitive multi-metal uptake and selectivity. Accordingly, this study aimed to (i) produce and characterize a matched series of pyrolysis-derived biochar and carbon-dot materials from date palm leaf waste subjected to ozonization, nutrient doping, or both, and (ii) comparatively evaluate how these post-pyrolysis treatments govern the sorption of $Pb^{2+}$, $Cd^{2+}$, $Mn^{2+}$ and $Zn^{2+}$ from aqueous solutions as a function of solution pH, adsorbent dose, initial metal concentration and contact time.

## 2. Materials and Methods

### 2.1. Feedstock Collection and Preparation

Date palm (*Phoenix dactylifera* L.) leaf waste was collected during routine annual pruning of mature orchards in Riyadh, Saudi Arabia. Fresh leaves were transported to the laboratory in sealed polyethylene bags, washed repeatedly with deionized water to remove adhering dust, sand and soluble surface salts and air-dried at ambient laboratory temperature for 7 d until constant weight. The dried material was chopped into 2–3 cm segments, homogenized by coning and quartering and stored in airtight containers at room temperature until further processing. A representative subsample of the untreated feedstock was retained and designated as biomass (BM) so that the effect of each subsequent thermal and chemical treatment could be referenced against the parent material.

### 2.2. Synthesis of Biochar and Carbon Dots

The prepared feedstock was pyrolyzed in a muffle furnace (Carbolite Model 3216, UK) at 500 °C for 2 h under a limited oxygen atmosphere, with the furnace purged before heating and the material held in closed crucibles to restrict air ingress. After pyrolysis, the furnace was allowed to cool to room temperature and

the resulting biochar (BC) recovered and stored in a desiccator over silica gel to prevent moisture uptake. The BC was subsequently milled for 1 h at 500 rpm in a planetary ball-milling unit (Fritsch Pulverisette 7, Germany) and passed through a sieve to obtain a uniform particle size of approximately 600 μm, thereby standardizing the particle size across all treatments so that differences in sorption could not be attributed to granulometry.

Carbon dot (CD) composites were generated from milled BC using a hydrothermal route adapted from Ahmad et al. (2020). Briefly, 10 g of BC and 2 g of citric acid ($C_6H8O_7$) were suspended in 300 mL of 6% hydrogen peroxide ($H_2O_2$), in which citric acid served as the supplementary carbon and carboxyl source and $H_2O_2$ served as the oxidant promoting fragmentation of the carbon skeleton. The suspension was stirred magnetically for 3 h at room temperature to ensure complete homogenization and then transferred to a Teflon-lined stainless-steel hydrothermal reactor. The sealed reactor was heated at 180 °C for 2 h in a pre-heated furnace and cooled passively to room temperature. The resulting CD composites were separated from the supernatant by centrifugation at 10,000 rpm, rinsed sequentially with methanol and deionized water to remove unreacted citric acid and soluble by-products and oven-dried at 50 °C until constant weight.

### 2.3. Ozonization

Freshly prepared BC and CD were subjected to gas-phase ozonization following the procedure described by Kharel et al. (2019). Oxygen from a compressed cylinder was passed through a corona-discharge ozone generator and the ozone-enriched stream was directed through a closed borosilicate glass vessel in which BC and CD were treated individually. The ozone flow rate was maintained at 3 L $min^{-1}$ under a pressure of 8 Pa for 90 min at room temperature. The vessel was shaken intermittently every 15 min at 140 rpm to disrupt channelling and ensure uniform gas-solid contact throughout the packed bed. After treatment, residual ozone was purged from the vessel with nitrogen, and the products were transferred to a desiccator. The ozonized materials were designated OBC and OCD.

### 2.4. Nutrient Doping

The synthesized BC, CD, OBC and OCD were subjected to nutrient doping with N, P and K, following An et al. (2020). A doping solution was prepared by dissolving 2.83% ammonium nitrate (NH4NO3) and 1.02% potassium dihydrogen phosphate (KH2PO4) in deionized water at room temperature and the solution pH was adjusted to 6.5 to keep the phosphate predominantly in the H2PO4- form and to avoid precipitation of sparingly soluble phosphate phases. Thereafter, 10 g of each material was individually submerged in 100 mL of freshly prepared nutrient solution in a 250 mL beaker. The suspension was stirred for 12 h and then held static for a further 72 h to allow the nutrient ions to diffuse into the internal pore network and equilibrate with the surface. The doped materials were recovered by precipitation followed by vacuum filtration and excess unbound nutrients removed by repeated washing with deionized water until the electrical conductivity of the filtrate stabilized. The nutrient-doped products were designated NBC, NCD, NOBC and NOCD, yielding eight materials (BC, CD, OBC, OCD, NBC, NCD, NOBC and NOCD) for subsequent characterization and sorption testing.

### 2.5. Rationale for Materials Engineering

The three treatments imposed in this study were selected because each target a distinct and independently documented control of metal sorption, allowing their individual and combined contributions to be separated within one factorial series. Pyrolysis at 500 °C was adopted because this temperature range maximizes the development of micro- and mesoporosity and aromaticity in lignocellulosic feedstocks while retaining a

workable population of oxygen-containing surface groups, whereas higher temperatures progressively volatilize these groups and depress cation exchange capacity (Gale et al., 2021; Xie et al., 2021). Ozonization was selected in preference to conventional acid or alkali oxidation because gaseous ozone cleaves aromatic C=C bonds and installs carboxylic and carbonyl functionality directly at the particle surface without generating acidic effluent or dissolving the mineral fraction. It has been shown to increase the cation exchange capacity of biochar by an order of magnitude (Huff et al., 2018; Eldeeb et al., 2024; Kharel et al., 2019). Nutrient doping with N, P and K was included because heteroatom incorporation introduces electron-donating nitrogen sites and phosphate ligands that promote inner-sphere complexation and surface precipitation of divalent metals and because loading a sorbent with plant-available nutrients confers secondary agronomic value on the spent material (Yuan et al., 2022; Ahmad et al., 2023). The carbon dot route was applied in parallel to bulk biochar because nanoscale carbon domains expose a far greater edge-site density per unit mass than the parent char (Ahmad et al., 2020; Chen et al., 2022). Therefore, applying ozonization and nutrient doping, both singly and in combination, to both the biochar and carbon dot platform was necessary to establish whether the two surface modifications acted additively on a common feedstock.

### 2.6. Characterization of the Synthesized Materials

All characterizations were performed on oven-dried, ball-milled subsamples and every determination was carried out in triplicate. Analytical-grade reagents and deionized water were used throughout, unless otherwise stated.

#### *2.6.1. Chemical and Proximate Properties*

The pH of each material was measured in a 1:10 (w/v) material-to-water suspension that was shaken for 1 h and allowed to stand for 30 min, using a calibrated pH meter (UP-10, Denver Instrument, USA) standardized against pH 4.0, 7.0 and 10.0 buffers before each batch (Gale et al., 2021). Electrical conductivity (EC) was determined in the supernatant of the same suspension with a conductance meter (YSI Model 35, USA) calibrated with 0.01 M KCl and reported at 25 °C. Cation exchange capacity (CEC) was determined using the ammonium acetate saturation method, in which 1 g of material was leached repeatedly with 1 N ammonium acetate buffered at pH 7.0, the excess saturating solution was displaced with ethanol and the adsorbed NH4+ was subsequently displaced and quantified by distillation, following the modified protocol recommended for carbonaceous materials by Munera-Echeverri et al. (2018). Proximate composition was determined according to ASTM D1762-84 (ASTM International, 1989).

#### *2.6.2. Nutrient Analysis*

Nitrate ($NO_3^-$) and ammonium ($NH_4^+$) were extracted and determined colorimetrically following the standard procedures of State Environmental Protection Administration of China (2002), using the appropriate color-developing reagents and reading absorbance on an ultraviolet-visible spectrophotometer (UV/VIS Lambda EZ 150, Germany) at 410 nm and 420 nm, respectively; total N was taken as the sum of the two mineral fractions. Total P was released by wet digestion (Olsen and Sommers, 1982) and quantified using the ascorbic acid-molybdenum blue procedure at 882 nm on the same spectrophotometer, with concentrations read against a calibration series prepared from a certified KH2PO4 standard. Total K was determined in the same digest by flame photometry following the standard method described by Banerjee and Prasad (2020), calibrated with KCl standards spanning the expected concentration range.

#### *2.6.3. Fourier Transform Infrared Spectroscopy*

Surface functional groups were identified by Fourier transform infrared spectroscopy using an attenuated total reflectance instrument (Bruker Alpha-Eco ATR-FTIR, Bruker Optics Inc., Germany). Oven-dried samples were pressed directly against the ATR crystal, and spectra were recorded over the 4000 to 400 $cm^{-1}$ range at a resolution of 4 $cm^{-1}$ with 32 co-added scans per sample. A background spectrum was collected against a clean crystal before each measurement and band assignments were made by reference to published spectra for lignocellulosic and carbonaceous materials.

*2.6.4. X-ray Diffraction Analysis*

The mineralogical composition and degree of structural ordering were assessed using an X-ray diffractometer (MAXima X XRD-7000, Shimadzu, Japan) operated with Cu-Kα radiation. Finely ground samples were packed into a zero-background holder and scanned over a 2θ range of 5° to 80° at a continuous scan rate and crystalline phases were identified by matching the observed reflections against standard reference patterns.

*2.6.5. Surface Area and Porosity*

The specific surface area, total pore volume and average pore diameter were determined from nitrogen adsorption-desorption isotherms measured at 77 K using a surface area and porosity analyzer. The samples were degassed under vacuum at 150 °C for 6 h before analysis to remove adsorbed moisture and volatiles. The specific surface area was calculated using the Brunauer-Emmett-Teller (BET) method over the relative pressure range appropriate for microporous carbons, the total pore volume was obtained from the quantity adsorbed at a relative pressure approaching unity and the average pore diameter was derived from the BET surface area and total pore volume.

*2.6.6. Surface Morphology and Elemental Composition*

The surface morphology was examined by scanning electron microscopy (SEM) coupled with energy-dispersive X-ray spectroscopy (EDX). The samples were mounted on aluminum stubs with double-sided carbon tape and sputter-coated with a thin conductive layer before imaging to suppress charging. Micrographs were acquired at several magnifications to resolve both the bulk texture and fine surface features, and EDX spectra were collected from representative fields to obtain the semi-quantitative elemental composition of each material.

2.7. Batch Adsorption Experiments

Batch-scale adsorption experiments were conducted to evaluate the capacity of the synthesized materials to remove $Pb^{2+}$, $Cd^{2+}$, $Mn^{2+}$ and $Zn^{2+}$ from a multi-metal aqueous solution. Stock solutions of 1000 mg $L^{-1}$ were prepared for each metal from analytical-grade $Pb(NO_3)_2$, $Cd(NO_3)_2$, $Mn(NO_3)_2$ and $Zn(NO_3)_2$ in deionized water, combined into a single multi-metal working solution containing all four metals and diluted to the required working concentrations immediately before use. All trials were run as multi-metal systems, in acid-washed polypropylene tubes at room temperature, in triplicate and with adsorbent-free controls included at every level to account for losses by precipitation or container-wall sorption. The effects of initial solution pH, adsorbent dose, initial metal concentration and contact time were examined sequentially, with the optimum conditions identified at each stage carried forward to the next.

*2.7.1. Effect of Initial Solution pH on Pb2+, Cd2+, Mn2+ and Zn2+ Sorption*

A multi-metal working solution containing 100 mg $L^{-1}$ of each of $Pb^{2+}$, $Cd^{2+}$, $Mn^{2+}$ and $Zn^{2+}$ was prepared by combining the respective nitrate stocks. The pH of separate portions of this solution was adjusted to 3,

5 and 7 using 1 M HCl and 1 M NaOH and the pH was re-checked and readjusted immediately before the adsorbent was added. A 50 mL aliquot of each pH-adjusted multi-metal solution was transferred to a polypropylene tube and 1 g $L^{-1}$ of each synthesized material was added separately. The suspensions were shaken at 150 rpm on a reciprocal shaker for 24 h to ensure equilibrium was attained and then filtered through Whatman 42 filter paper. The residual concentrations of $Pb^{2+}$, $Cd^{2+}$, $Mn^{2+}$ and $Zn^{2+}$ in the filtrate were determined by ICP-OES and the removal efficiency was calculated from the difference between the initial and equilibrium concentrations.

### *2.7.2. Effect of Adsorbent Dose on $Pb^{2+}$, $Cd^{2+}$, $Mn^{2+}$ and $Zn^{2+}$ Sorption*

To assess the influence of sorbent loading, each synthesized material was applied at 0.5, 1 and 2 g $L^{-1,}$ together with an adsorbent-free control at 0 g $L^{-1}$, to 50 mL of the multi-metal solution containing 100 mg $L^{-1}$ of each of $Pb^{2+}$, $Cd^{2+}$, $Mn^{2+}$ and $Zn^{2+}$ at the optimum pH identified in Section 2.7.1. The suspensions were shaken at 150 rpm for 24 h, filtered through Whatman 42 filter paper and the residual metal concentrations in the filtrate were determined using ICP-OES.

### *2.7.3. Effect of Initial Metal Concentration on $Pb^{2+}$, $Cd^{2+}$, $Mn^{2+}$ and $Zn^{2+}$ Sorption*

To construct the sorption isotherms, multi-metal solutions with initial concentrations of 0, 5, 10, 20, 50 and 100 mg $L^{-1}$ of each of $Pb^{2+}$, $Cd^{2+}$, $Mn^{2+}$ and $Zn^{2+}$ were prepared. The pH and adsorbent dose were fixed at the optimum values established in Sections 2.7.1 and 2.7.2, respectively. After pH adjustment, each solution was combined with the prescribed mass of adsorbent and the suspensions were shaken at 150 rpm for 24 h, filtered through Whatman 42 filter paper and analyzed for residual $Pb^{2+}$, $Cd^{2+}$, $Mn^{2+}$ and $Zn^{2+}$ by ICP-OES. The equilibrium adsorbed quantity was then calculated and fitted to the isotherm models described in Section 2.7.5.

### *2.7.4. Effect of Contact Time on $Pb^{2+}$, $Cd^{2+}$, $Mn^{2+}$ and $Zn^{2+}$ Sorption*

Sorption kinetics were determined to establish the rates of $Pb^{2+}$, $Cd^{2+}$, $Mn^{2+}$ and $Zn^{2+}$ uptake and the time required to reach equilibrium for each metal. A multi-metal solution containing 100 mg $L^{-1}$ of each metal was prepared and adjusted to the optimum pH and 50 mL aliquots were combined with the optimum adsorbent dose and adsorbent-free controls. The suspensions were shaken continuously at 150 rpm, and subsamples were withdrawn at 0, 15, 30, 60, 120, 240, 480, 960 and 1440 min. Each subsample was filtered immediately through Whatman 42 filter paper to prevent further sorption and the residual concentrations of $Pb^{2+}$, $Cd^{2+}$, $Mn^{2+}$ and $Zn^{2+}$ were determined using ICP-OES.

### *2.7.5. Sorption Quantification and Equilibrium Isotherm Models*

The quantities of $Pb^{2+}$, $Cd^{2+}$, $Mn^{2+}$ and $Zn^{2+}$ adsorbed at equilibrium were calculated from the mass balance between the initial and equilibrium solution concentrations (Eq. 1) and the corresponding removal efficiency was expressed as a percentage of the initial concentration (Eq. 2). Because the four metals were present together, all isotherm and kinetic parameters describe the uptake of each metal in competition with the other three (competitive sorption).

$$Q_e = \frac{V(C_0 - C_e)}{m} \quad (1)$$

$$R\ (\%) = \frac{C_0 - C_e}{C_0} \times 100 \quad (2)$$

where $Q_e$ is the quantity of $Pb^{2+}$, $Cd^{2+}$, $Mn^{2+}$, or $Zn^{2+}$ adsorbed at equilibrium (mg $g^{-1}$), $C_0$ and $C_e$ are the initial and equilibrium metal concentrations in solution (mg $L^{-1}$), V is the volume of the metal solution (L), m is the mass of the adsorbent (g) and R is the removal efficiency (%).

The equilibrium sorption data were fitted to the non-linear forms of the Langmuir (Eq. 3), Freundlich (Eq. 4), Temkin (Eq. 5) and Dubinin-Radushkevich (DR; Eq. 6) isotherm models, with the Polanyi potential defined by Eq. 7 (Mohan et al., 2011; Okpara et al., 2021). The model parameters were estimated using non-linear least-squares regression and the goodness of fit of each model was assessed from the coefficient of determination.

$$Q_e = \frac{Q_L K_L C_e}{1 + K_L C_e} \quad (3)$$

$$Q_e = K_F C_e^{\frac{1}{n}} \quad (4)$$

$$Q_e = \frac{RT}{b_T} \ln(A_T C_e) \quad (5)$$

$$q_e = q_m \exp(-\beta \varepsilon^2) \quad (6)$$

$$\varepsilon = RT \ln\left(1 + \frac{1}{C_e}\right) \quad (7)$$

where $Q_L$ is the Langmuir maximum monolayer sorption capacity (mg $g^{-1}$), $K_L$ is the Langmuir affinity constant (L $mg^{-1}$), $K_F$ is the Freundlich capacity parameter (mg $g^{-1}$ (L $mg^{-1}$)1/n), 1/n is the Freundlich intensity parameter, $A_T$ is the Temkin equilibrium binding constant (L $mg^{-1}$), $b_T$ is the Temkin constant related to the heat of sorption (J $mol^{-1}$), $q_m$ is the Dubinin-Radushkevich sorption capacity (mg $g^{-1}$), β is the activity coefficient related to the mean free energy of sorption ($mol^2$ $kJ^{-2}$), ε is the Polanyi potential, R is the universal gas constant ($8.314 \times 10^{-3}$ kJ $mol^{-1}$ $K^{-1}$) and T is the absolute temperature (K).

*2.7.6. Sorption Kinetic Models*

The time-dependent sorption data were fitted to six kinetic expressions to characterize the rate-controlling step: first-order (Eq. 8), pseudo-first-order (Eq. 9), pseudo-second-order (Eq. 10), intraparticle diffusion (Eq. 11), power function (Eq. 12) and Elovich (Eq. 13) models, following the procedures described by Sparks (1998). The rate constants were obtained by regression of the linearized forms and the model with the highest coefficient of determination was considered the best descriptor of the uptake mechanism.

$$\ln q_t = \ln q_0 - k_1 t \quad (8)$$

$$\ln(q_e - q_t) = \ln q_e - k_1 t \quad (9)$$

$$\frac{t}{q_t} = \frac{1}{k_2 q_e^2} + \frac{t}{q_e} \quad (10)$$

$$q_t = a + k_{id} t^{0.5} \quad (11)$$

$$\ln q_t = \ln b + k_f \ln t \quad (12)$$

$$q_t = \frac{1}{\beta} \ln(\alpha\beta) + \frac{1}{\beta} \ln t \quad (13)$$

where $q_t$ and $q_0$ are the quantities of $Pb^{2+}$, $Cd^{2+}$, $Mn^{2+}$, or $Zn^{2+}$ adsorbed (mg $g^{-1}$) at time t (min) and at t = 0, respectively, $q_e$ is the quantity adsorbed at equilibrium (mg $g^{-1}$), $k_1$ is the first-order rate constant ($min^{-1}$), $k_2$ is the pseudo-second-order rate constant (g $mg^{-1}$ $min^{-1}$), $k_{id}$ is the intraparticle diffusion rate constant (mg

$g^{-1}$ $min^{-0.5}$), $k_f$ is the power function exponent, a and b are model constants, α is the initial sorption rate of the Elovich model (mg $g^{-1}$ $min^{-1}$) and β is the Elovich desorption constant (g $mg^{-1}$).

2.8. Statistical Analysis

All treatments were arranged in a completely randomized design with three independent replicates, and each analytical determination was performed in triplicate. Isotherm and kinetic model parameters were estimated using least-squares regression and model performance was compared using the coefficient of determination. All analyses were conducted in SigmaPlot and Statistix 8.1, following the procedures described by Steel et al. (1997).

## 3. Results

3.1. Characterization

*3.1.1. Chemical and proximate analyses*

The pyrolysis shifted the carbon materials from a mildly acidic, volatile-rich biomass toward an alkaline, carbon-dense solid and the subsequent surface treatment amplified the exchange capacity without reversing this shift (Table 1). The reaction pH rose from 5.46 in BM to 9.27 in BC, crossing from the acidic into the strongly alkaline range, while EC spanned 0.36 to 3.42 dS $m^{-1,}$ with the minimum in CD and the maximum in BC. CEC increased mainly as a function of ozonization rather than of overall treatment intensity, from 69.357 $cmol_c$ $kg^{-1}$ in the untreated biomass to 122.914 $cmol_c$ $kg^{-1}$ in NOCD, a 1.8-fold gain that tracked the combined ozonization and nutrient-doping sequence. The proximate composition shifted in the opposite direction to the volatile content: volatile matter fell from 82.310% in BM to 17.923% in BC and 6.053% in CD, whereas fixed carbon rose from 6.018% to a maximum of 62.18% in NOCD, a tenfold enrichment. ash rose sharply with pyrolysis itself and was not further increased by doping, peaking at 23.756% in NOBC while remaining at 19.698% in NBC, close to or below the 23.567% already present in undoped BC and moisture remained below 5% in all synthesized materials (the untreated biomass was higher, at 6.368%), ranging from 2.654% in BC to 4.882% in OCD.

Nutrient doping only partially compensates the nitrogen loss imposed by pyrolysis, while markedly enriching phosphorus relative to the parent biomass (Table 2). The total N content collapsed from 4056.31 mg $kg^{-1}$ in BM to 27.26 to 39.33 mg $kg^{-1}$ across BC, OBC, CD and OCD, a loss of two orders of magnitude that thermal treatment alone could not reverse. Total P content moved in the opposite direction, rising from a minimum of 967.96 mg $kg^{-1}$ in BM to 1758.48 and 1800.66 mg $kg^{-1}$ in BC and OBC, respectively and reaching 4491.50 mg $kg^{-1}$ in NCD and 4704.75 mg $kg^{-1}$ in NBC, a 4.9-fold enrichment over the feedstock.

**Table 1** Chemical properties and proximate composition of date palm leaf biomass and the eight synthesized carbon materials

| Sample | pH | EC (dS $m^{-1}$) | CEC ($cmol_c$ $kg^{-1}$) | Moisture (%) | Volatile material (%) | Ash (%) | Fixed carbon |
|---|---|---|---|---|---|---|---|
| BM | 5.46 | 2.90 | 69.357 | 6.368 | 82.310 | 5.304 | 6.018 |
| BC | 9.27 | 3.42 | 71.752 | 2.654 | 17.923 | 23.567 | 55.856 |
| OBC | 7.71 | 3.76 | 122.661 | 2.713 | 21.573 | 23.552 | 52.162 |
| NOBC | 7.19 | 1.67 | 121.103 | 4.138 | 22.924 | 23.756 | 49.182 |
| NBC | 7.28 | 1.12 | 71.693 | 4.071 | 21.852 | 19.698 | 54.379 |
| CD | 6.85 | 0.36 | 85.468 | 4.861 | 6.053 | 19.901 | 69.185 |
| OCD | 6.32 | 0.38 | 120.253 | 4.882 | 13.392 | 20.547 | 61.179 |
| NOCD | 5.97 | 1.14 | 122.914 | 4.310 | 12.51 | 21.000 | 62.18 |
| NCD | 5.865 | 1.91 | 86.687 | 4.399 | 27.194 | 21.928 | 46.479 |

Note. EC: electrical conductivity; CEC: cation-exchange capacity. BM, date palm leaf biomass; BC, biochar; OBC, ozonized biochar; NBC, nutrient-doped biochar; NOBC, nutrient-doped ozonized biochar; CD, carbon dots; OCD, ozonized carbon dots; NCD, nutrient-doped carbon dots; NOCD, nutrient-doped ozonized carbon dots.

**Table 2** Total nitrogen, phosphorus and potassium concentrations (mg $kg^{-1}$) of date palm leaf biomass and the synthesized and modified carbon materials.

| Sample | Total N | Total P | Total K |
|---|---|---|---|
| | (mg $kg^{-1}$) | | % |
| BM | 4056.31 | 967.96 | 1.00 |
| BC | 30.39 | 1758.48 | 1.91 |
| OBC | 37.96 | 1800.66 | 1.85 |
| NOBC | 630.47 | 4633.67 | 3.04 |
| NBC | 646.77 | 4704.75 | 3.74 |
| CD | 27.26 | 1552.88 | 1.57 |
| OCD | 39.33 | 1662.56 | 1.74 |
| NOCD | 776.26 | 4146.24 | 2.93 |
| NCD | 705.34 | 4491.50 | 3.16 |

Note. Values are expressed on a dry-mass basis. BM, date palm leaf biomass; BC, biochar; OBC, ozonized biochar; NBC, nutrient-doped biochar; NOBC, nutrient-doped ozonized biochar; CD, carbon dots; OCD, ozonized carbon dots; NCD, nutrient-doped carbon dots; NOCD, nutrient-doped ozonized carbon dots.

*3.1.2. FTIR Analysis*

Pyrolysis progressively stripped the oxygen-rich aliphatic functionality from the feedstock, whereas post-synthesis treatments reinstated the mineral- and oxygen-associated bands (Fig. 1). The broad O-H stretching envelope at 3200–3600 $cm^{-1,}$ prominent in BM, largely disappeared in BC, OBC, NBC and NOBC. Bands near 1600 $cm^{-1,}$ assigned to aromatic C=C stretching or the bending of adsorbed water, persisted in BM, OBC and NOBC but weakened in BC and the composites. The aliphatic C-H and carboxylate O-C =O features at 1380–1440 cm-1 were weak in BC, NBC, NCD and NOBC. Sharp bands at 1030–1100 $cm^{-1,}$ attributable to C–O–C, C–O and Si–O vibrations, were prominent in CD, OBC, OCD and NOBC, absent in BM and BC and reappeared in NCD and NOCD, indicating that these features tracked ozonization and doping rather than pyrolysis. Weak aromatic C-H bending bands at 870–890 $cm^{-1}$ were recorded across the treated materials.

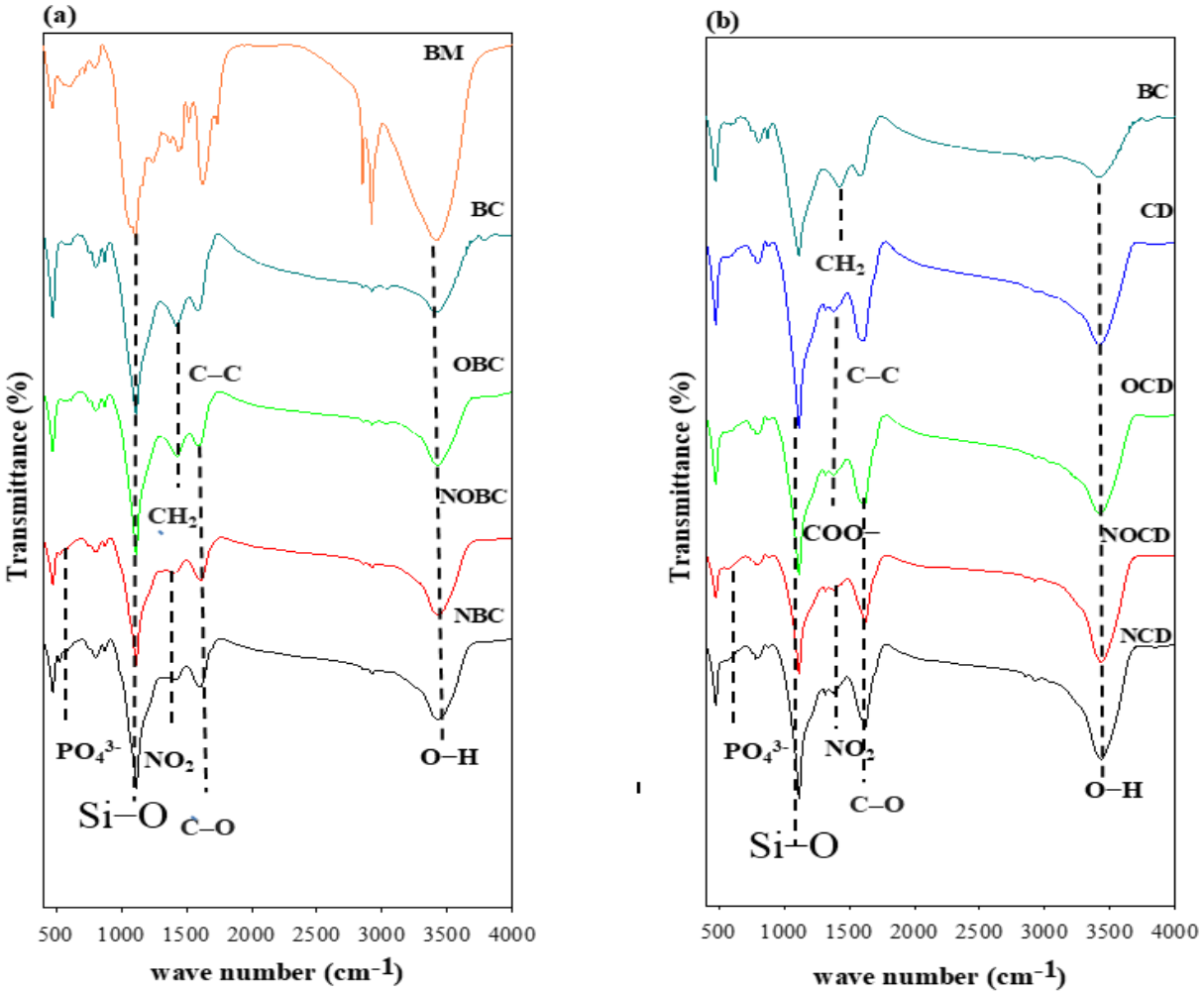



**Fig. 1** Fourier-transform infrared (FTIR) spectra of (a) date palm leaf biomass (BM), biochar (BC), ozonized biochar (OBC), nutrient-doped biochar (NBC) and nutrient-doped ozonized biochar (NOBC) and (b) biochar (BC), carbon dots (CD), ozonized carbon dots (OCD), nutrient-doped carbon dots (NCD) and nutrient-doped ozonized carbon dots (NOCD).

*3.1.3. XRD Analysis*

Crystallinity increased progressively from amorphous biomass to carbonized and surface-treated materials (Fig. 2). BM produced a broad hump at 2θ = 20° to 30°, characteristic of amorphous organic matter and BC retained a similar but weaker and slightly shifted feature. OBC and NBC resolved into sharper reflections at 2θ ≈ 26.6°, 29.4°, 31° to 33° and 36°, consistent with quartz ($SiO_2$), calcite ($CaCO_3$) and metal oxides ($Fe_2O_3$, $MnO_2$). Within the carbon dot series, CD showed a broad peak near 2θ ≈ 24° corresponding to the (002) plane of turbostratic graphitic carbon, whereas OCD and NOCD developed defined reflections at 2θ ≈ 26.6°, 30° and 36°. OCD and NOCD were the most crystalline materials of the series, with prominent peaks across 2θ = 20° to 60° and a major reflection near 30.5°.

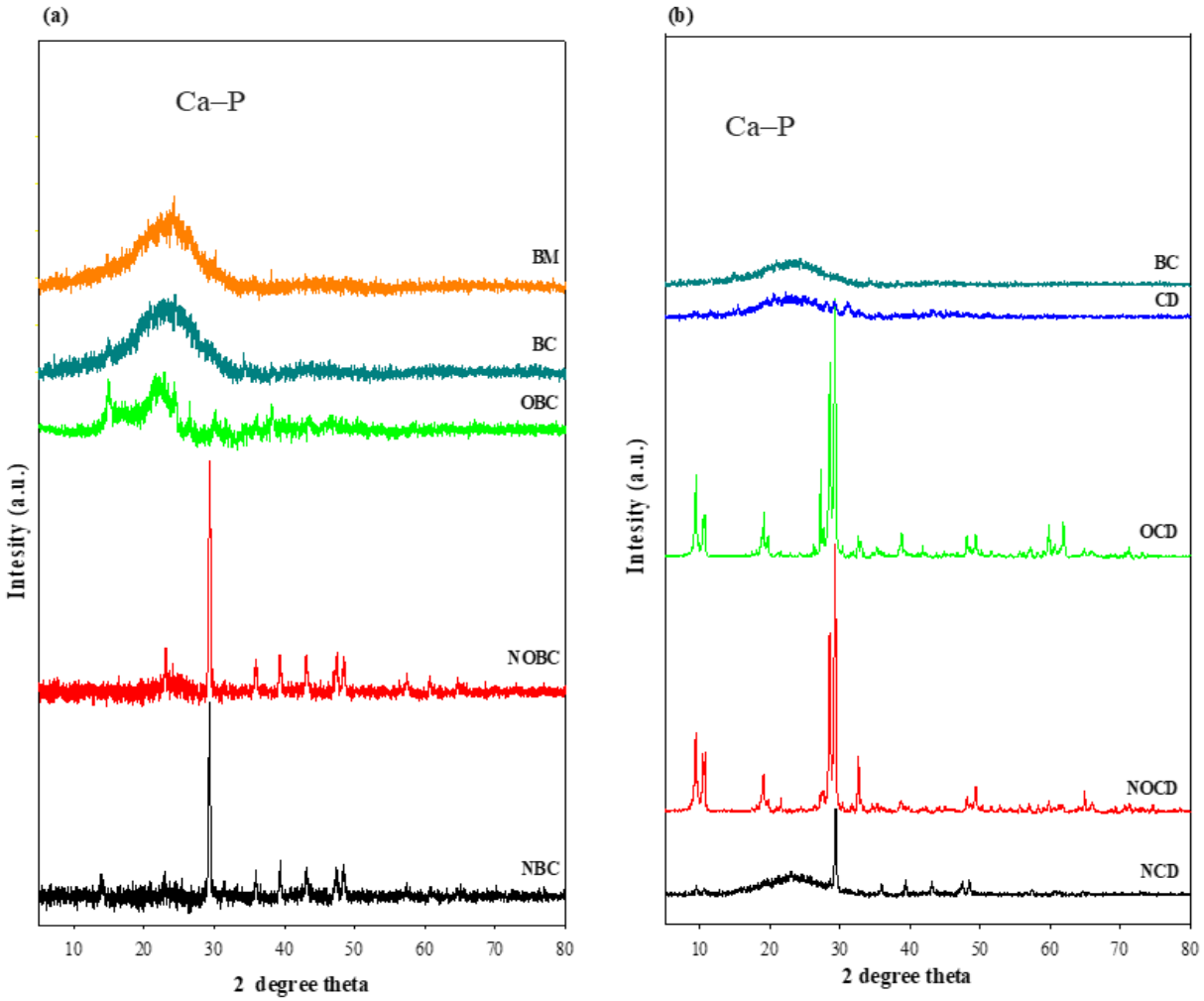



**Fig. 2** X-ray diffraction (XRD) patterns of (a) date palm leaf biomass (BM), biochar (BC), ozonized biochar (OBC), nutrient-doped biochar (NBC) and nutrient-doped ozonized biochar (NOBC) and (b) biochar (BC), carbon dots (CD), ozonized carbon dots (OCD), nutrient-doped carbon dots (NCD) and nutrient-doped ozonized carbon dots (NOCD).

*3.1.4. Surface Area and Morphology*

Pyrolysis was the dominant factor controlling porosity development and every subsequent surface treatment reduced the accessible surface area relative to that of the parent material (Table 3). The surface area increased twelvefold from 4.30 $m^2 g^{-1}$ in BM to 52.32 $m^2 g^{-1}$ in BC and reached 62.50 $m^2 g^{-1}$ in CD, while the average pore size widened from approximately 9.1 to 18.48 Å and the pore volume increased from 0.00098 to 0.00799 $cm^3 g^{-1}$. Ozonization and nutrient doping reversed this gain, lowering the surface area to 14.60–34.22 $m^{2\ g\text{-}1}$ and the pore volume to 0.0011–0.00461 $cm^3 g^{-1}$, with the steepest loss recorded under nutrient doping. The carbon dot series was affected most severely, with all modified variants falling to 14.72–17.88 $m^2 g^{-1}$, approximately one-quarter of the unmodified CD surface area.

**Table 3** Brunauer–Emmett–Teller (BET) specific surface area, total pore volume and mean pore width of date palm leaf biomass and the synthesized carbon materials.

| Sample | BET surface area ($m^2/g$) | Pore volume ($cm^3/g$) | Pore size (Å) |
|---|---|---|---|
| BM | 4.30 | 0.00098 | 9.13 |
| BC | 52.32 | 0.00841 | 18.48 |
| OBC | 34.22 | 0.00461 | 18.53 |
| NOBC | 15.93 | 0.00236 | 18.62 |
| NBC | 14.60 | 0.00110 | 18.51 |
| CD | 62.50 | 0.00799 | 18.49 |
| OCD | 17.88 | 0.00213 | 18.60 |
| NOCD | 16.99 | 0.00219 | 18.54 |
| NCD | 14.72 | 0.00185 | 18.59 |

BET, Brunauer-Emmett-Teller. BM, date palm leaf biomass; BC, biochar; OBC, ozonized biochar; NBC, nutrient-doped biochar; NOBC, nutrient-doped ozonized biochar; CD, carbon dots; OCD, ozonized carbon dots; NCD, nutrient-doped carbon dots; NOCD, nutrient-doped ozonized carbon dots.

3.2. Heavy Metal Sorption Experiment

All sorption experiments were performed in a multi-metal solution containing $Pb^{2+}$, $Cd^{2+}$, $Mn^{2+}$ and $Zn^{2+}$ together (Section 2.7). Every removal efficiency, capacity and kinetic parameter reported below therefore describes the uptake of one metal in competition with the other three, and the results are interpreted in that competitive context.

*3.2.1. Effect of pH on Heavy Metal Removal*

The removal of all four metals increased with rising pH, peaked at pH 5 and declined thereafter, identifying pH 5 as the threshold beyond which further alkalinization reduced rather than enhanced metal loss from solution (Fig. 3). The steepness of this response differed sharply among metals, being greatest for $Pb^{2+}$ and negligible for $Mn^{2+}$.

$Pb^{2+}$ was the most efficiently removed metal across all adsorbents, spanning 43% for unmodified BC to 97% for NOCD; all ozonized and nutrient-doped materials exceeded 60%, whereas BC alone remained below 50%. $Cd^{2+}$ followed the same adsorbent ranking on a far lower plateau, peaking at 12% for NOCD and 8.3% for NOBC, with the remaining materials confined to 4.0 - 8.0%. $Mn^{2+}$ was the least pH-responsive metal, with removal remaining within 4–11% across the full pH range. $Zn^{2+}$ was intermediate, at 12% for BC to 20% for NOCD, a treatment spread roughly one-quarter of that recorded for $Pb^{2+}$. As all the four metals competed for the same binding sites, the higher sorption of $Pb^{2+}$ indicates that the sorbents retained $Pb^{2+}$ preferentially over $Zn^{2+}$, $Cd^{2+}$ and $Mn^{2+}$.

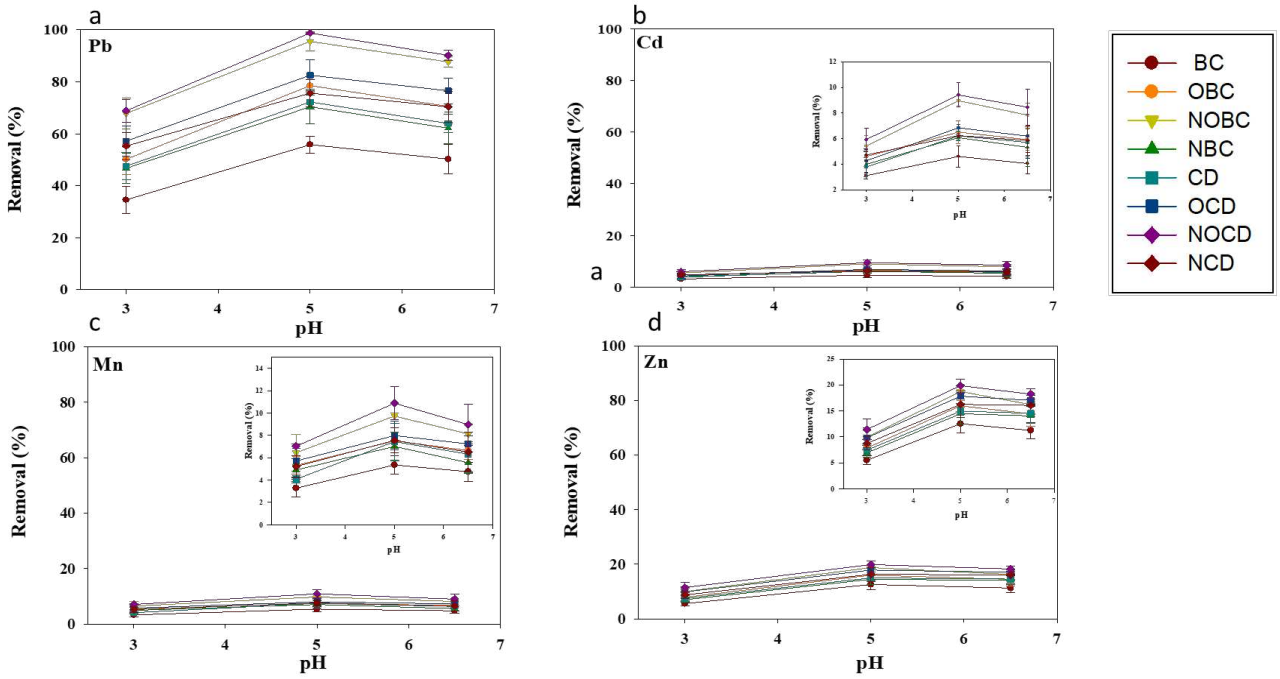



**Fig. 3** Effect of initial solution pH on the competitive sorption of (a) $Pb^{2+}$, (b) $Cd^{2+}$, (c) $Mn^{2+}$ and (d) $Zn^{2+}$ from a multi-metal solution onto biochar (BC), ozonized biochar (OBC), nutrient-doped biochar (NBC), nutrient-doped ozonized biochar (NOBC), carbon dots (CD), ozonized carbon dots (OCD), nutrient-doped carbon dots (NCD) and nutrient-doped ozonized carbon dots (NOCD).

*3.2.2. Effect of Adsorbent Dose on Heavy Metal Removal*

Removal efficiency did not respond monotonically to the adsorbent loading, rising between 0.5 and 1.0 g $L^{-1}$ and falling again to 2.0 g $L^{-1}$ for every material and metal, identifying 1.0 g $L^{-1}$ as the optimum dose (Fig. 4). $Pb^{2+}$ again showed the widest treatment contrast, spanning 53% for BC to 93% for NOCD and retained high removal even at the lowest dose. $Cd^{2+}$ remained confined to 3% to 9% across doses, with NOCD the strongest performer at 9% and BC the weakest at 3%. $Mn^{2+}$ tracked $Cd^{2+}$ closely, improving with dose across all adsorbents but reaching only 11% in NOCD. $Zn^{2+}$ spanned 12% for BC to 20% for NOCD, so that across all four metals NOCD consistently defined the upper bound of removal and unmodified BC the lower. This ranking held for all four metals although they competed for the same sites, so the advantage of NOCD was not lost under competition.

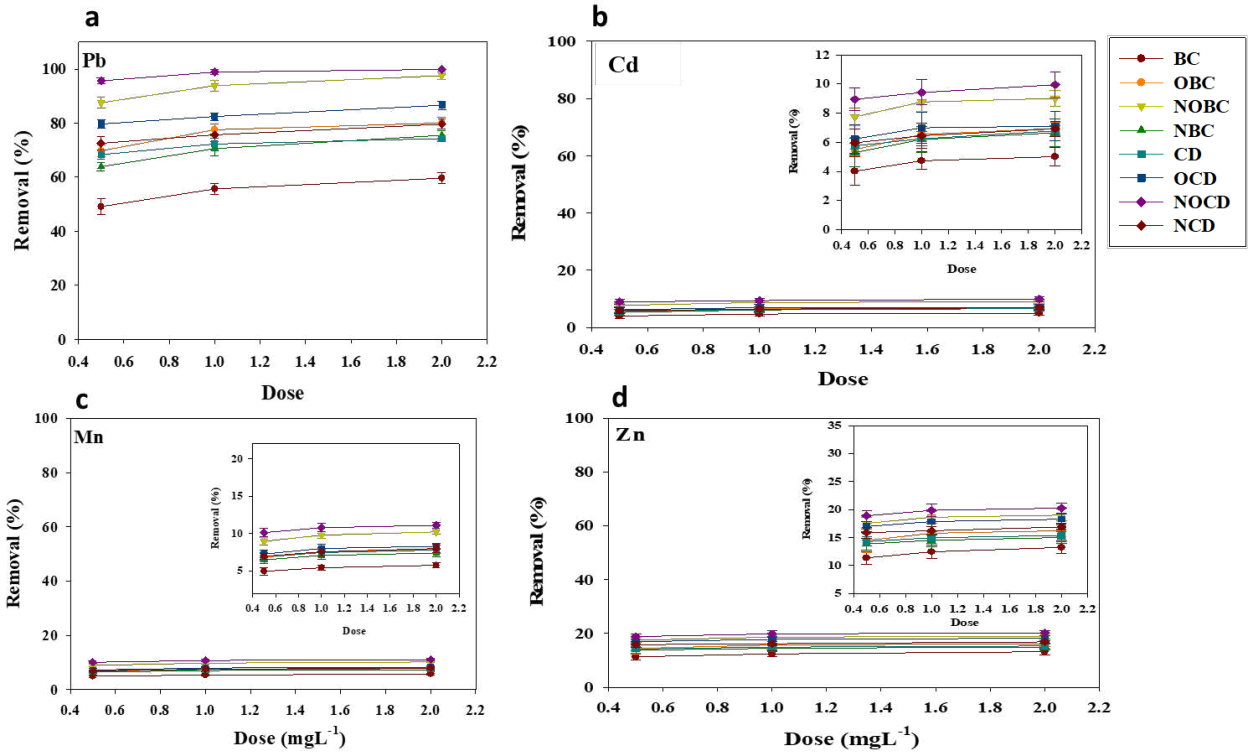



**Fig. 4** Effect of adsorbent dose on the competitive sorption of (a) $Pb^{2+}$, (b) $Cd^{2+}$, (c) $Mn^{2+}$ and (d) $Zn^{2+}$ from a multi-metal solution onto biochar (BC), ozonized biochar (OBC), nutrient-doped biochar (NBC), nutrient-doped ozonized biochar (NOBC), carbon dots (CD), ozonized carbon dots (OCD), nutrient-doped carbon dots (NCD) and nutrient-doped ozonized carbon dots (NOCD).

*3.2.3. Equilibrium Sorption*

Sorption increased steeply with initial metal concentration before levelling off, indicating that binding-site availability rather than solution supply limited uptake as equilibrium was approached. Isotherm trials were conducted at pH 5, the optimum identified above and, under these multi-metal conditions, the competitive sorption affinity sequence for NOCD was $Pb^{2+} > Zn^{2+} > Cd^{2+} > Mn^{2+}$ ($Pb^{2+}$ and $Zn^{2+}$ ranked first and second on every material, whereas the order of $Cd^{2+}$ and $Mn^{2+}$ varied among materials; Table 4). The Langmuir model best described $Pb^{2+}$ sorption, with $R^2$ of 0.94–0.99 and the Freundlich model also fitted the data for all four metals.

NOCD achieved the highest monolayer capacity for every metal tested, even in competition with the other three metals, confirming that the combined ozonization and nutrient-doping sequence, rather than either treatment alone, delivered the largest gain in effective binding site density (Fig. 5; Table 4). The maximum $Q_L$ followed the order $Pb^{2+}$ (138.31 mg $g^{-1}$) > $Zn^{2+}$ (22.02 mg $g^{-1}$) > $Cd^{2+}$ (15.13 mg $g^{-1}$) > $Mn^{2+}$ (12.96 mg $g^{-1}$), with a more than tenfold spread between the strongest and weakest metals.

Model fit remained strong across metals, with $R^2$ values of 0.91–0.99 for $Cd^{2+}$, 0.44–0.99 for $Mn^{2+}$ and 0.79–0.97 for $Zn^{2+}$. NCD recorded the highest $K_L$ for $Cd^{2+}$ (1.22 L $mg^{-1}$) and $Zn^{2+}$ (0.36 L $mg^{-1}$); NOCD returned the highest value for $Pb^{2+}$ (2.10 L $mg^{-1}$, reported above), and NCD showed the highest $K_L$ for $Mn^{2+}$ (6.21 L $mg^{-1}$).

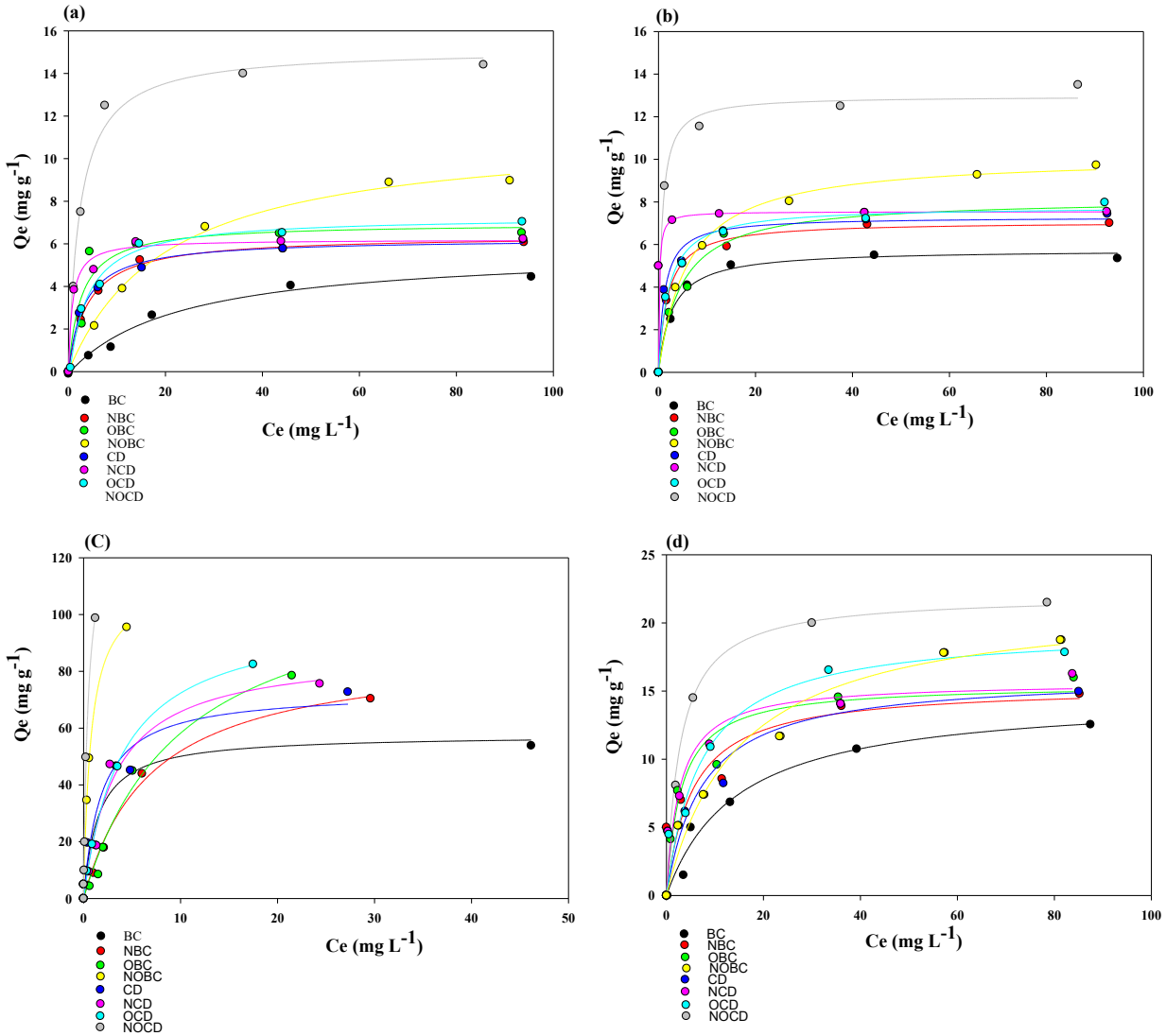



**Fig. 5** Langmuir isotherm fitting curves for the competitive sorption of (a) $Cd^{2+}$, (b) $Mn^{2+}$, (c) $Pb^{2+}$ and (d) $Zn^{2+}$ from a multi-metal solution onto biochar (BC), ozonized biochar (OBC), nutrient-doped biochar (NBC), nutrient-doped ozonized biochar (NOBC), carbon dots (CD), ozonized carbon dots (OCD), nutrient-doped carbon dots (NCD) and nutrient-doped ozonized carbon dots (NOCD).

**Table 4** Langmuir isotherm parameters for the competitive sorption of $Pb^{2+}$, $Cd^{2+}$, $Mn^{2+}$ and $Zn^{2+}$ from a multi-metal solution onto the synthesized carbon materials.

| Adsorbent | $Pb^{2+}$ | | | $Cd^{2+}$ | | | $Mn^{2+}$ | | | $Zn^{2+}$ | | |
|---|---|---|---|---|---|---|---|---|---|---|---|---|
| | $Q_L$ (mg $g^{-1}$) | $K_L$ (L $mg^{-1}$) | $R^2$ | $Q_L$ (mg $g^{-1}$) | $K_L$ (L $mg^{-1}$) | $R^2$ | $Q_L$ (mg $g^{-1}$) | $K_L$ (L $mg^{-1}$) | $R^2$ | $Q_L$ (mg $g^{-1}$) | $K_L$ (L $mg^{-1}$) | $R^2$ |
| **BC** | 57.62 | 0.66 | 0.94 | 5.86 | 0.04 | 0.98 | 5.75 | 0.36 | 0.99 | 14.67 | 0.06 | 0.97 |
| **NBC** | 87.87 | 0.14 | 0.99 | 6.38 | 0.24 | 0.99 | 7.07 | 0.53 | 0.99 | 15.35 | 0.18 | 0.79 |
| **OBC** | 117.08 | 0.09 | 0.98 | 6.95 | 0.37 | 0.91 | 8.15 | 0.21 | 0.99 | 15.49 | 0.32 | 0.95 |
| **NOBC** | 112.27 | 1.31 | 0.99 | 11.33 | 0.04 | 0.99 | 10.14 | 0.16 | 0.99 | 21.78 | 0.06 | 0.97 |
| **CD** | 73.03 | 0.54 | 0.96 | 6.23 | 0.30 | 0.99 | 7.28 | 0.82 | 0.99 | 16.16 | 0.13 | 0.87 |
| **NCD** | 87.09 | 0.30 | 0.97 | 6.19 | 1.22 | 0.99 | 7.54 | 6.21 | 0.44 | 15.66 | 0.36 | 0.93 |
| **OCD** | 100.74 | 0.25 | 0.99 | 7.08 | 0.25 | 0.99 | 7.78 | 0.47 | 0.99 | 19.56 | 0.14 | 0.96 |
| **NOCD** | 138.31 | 2.10 | 0.99 | 15.13 | 0.42 | 0.99 | 12.96 | 1.57 | 0.81 | 22.02 | 0.35 | 0.97 |

Note. $Q_L$, Langmuir monolayer sorption capacity; $K_L$, Langmuir affinity constant; $R^2$, coefficient of determination. BM, date palm leaf biomass; BC, biochar; OBC, ozonized biochar; NBC, nutrient-doped biochar; NOBC, nutrient-doped ozonized biochar; CD, carbon dots; OCD, ozonized carbon dots; NCD, nutrient-doped carbon dots; NOCD, nutrient-doped ozonized carbon dots.

All adsorbents returned 1/n values (Freundlich model) below unity and the NOCD advantage observed in the Langmuir model persisted (Fig. S1; Table S1: Supplementary Material). NOCD recorded the maximum $K_F$ for every metal, reaching 90.166 mg $g^{-1}$ (L $mg^{-1}$)$^{1/n}$ for $Pb^{2+}$ and 6.345, 8.934 and 8.446 L $mg^{-1}$ for $Cd^{2+}$, $Mn^{2+}$ and $Zn^{2+}$ mg $g^{-1}$ (L $mg^{-1}$)$^{1/n}$, respectively, with $Cd^{2+}$ fits returning $R^2$ values of 0.84 to 0.99.

The Temkin model returned high coefficients of determination but internally inconsistent parameters, with binding constants did not scale coherently with treatment intensity; therefore, it was not used to rank the adsorbents (Fig. S2). Because the derived binding constants were not physically meaningful across adsorbents, the full Temkin parameter set is reported in the Supplementary Material (Table S2) rather than interpreted here.

The DR model reproduced the adsorbent ranking obtained under the Langmuir model, returning the highest $q_m$ for NOCD across all tested metals (Fig. S3; Table 5). The maximum $q_m$ for $Pb^{2+}$ ranged from 54.61 mg $g^{-1}$ in BC to 120.12 mg $g^{-1}$ in NOCD, a 2.2-fold contrast between the least and most modified materials and NOCD likewise recorded the highest $q_m$ for $Cd^{2+}$, $Mn^{2+}$ and $Zn^{2+}$ at 13.51, 12.57 and 19.77 mg $g^{-1,}$ respectively. The values of β spanned 0.0001–0.0447 $mol^2$ $kJ^{-2}$ across all adsorbents.

**Table 5** Dubinin-Radushkevich isotherm parameters for the competitive sorption of $Pb^{2+}$, $Cd^{2+}$, $Mn^{2+}$ and $Zn^{2+}$ from a multi-metal solution onto the synthesized carbon materials

| Adsorbent | $Pb^{2+}$ | | | $Cd^{2+}$ | | | $Mn^{2+}$ | | | $Zn^{2+}$ | | |
|---|---|---|---|---|---|---|---|---|---|---|---|---|
| | $q_m$ (mg $g^{-1}$) | β (mol$^2$ $kJ^{-2}$) | $R^2$ | $q_m$ (mg $g^{-1}$) | β (mol$^2$ $kJ^{-2}$) | $R^2$ | $q_m$ (mg $g^{-1}$) | β (mol$^2$ $kJ^{-2}$) | $R^2$ | $q_m$ (mg $g^{-1}$) | β (mol$^2$ $kJ^{-2}$) | $R^2$ |
| BC | 54.61 | 0.0009 | 0.93 | 4.41 | 0.0447 | 0.92 | 5.25 | 0.0022 | 0.96 | 10.81 | 0.01 | 0.87 |
| NBC | 64.34 | 0.0029 | 0.93 | 5.57 | 0.0028 | 0.87 | 6.45 | 0.0009 | 0.84 | 12.78 | 0.0026 | 0.58 |
| OBC | 73.25 | 0.0031 | 0.95 | 6.57 | 0.0027 | 0.88 | 6.84 | 0.0025 | 0.75 | 13.16 | 0.0008 | 0.72 |
| NOBC | 97.87 | 0.0002 | 0.99 | 8.49 | 0.0311 | 0.89 | 8.69 | 0.0049 | 0.81 | 16.97 | 0.0225 | 0.69 |
| CD | 59.80 | 0.0002 | 0.85 | 5.45 | 0.0018 | 0.77 | 6.74 | 0.0004 | 0.75 | 13.12 | 0.0056 | 0.53 |
| NCD | 74.72 | 0.0013 | 0.97 | 5.88 | 0.0003 | 0.76 | 7.51 | 0.0002 | 0.96 | 14.28 | 0.0023 | 0.65 |
| OCD | 83.97 | 0.003 | 0.86 | 6.06 | 0.0022 | 0.77 | 6.95 | 0.0008 | 0.77 | 13.19 | 0.0003 | 0.44 |
| NOCD | 120.12 | 0.0001 | 0.98 | 13.51 | 0.0010 | 0.91 | 12.57 | 0.0003 | 0.87 | 19.77 | 0.0017 | 0.84 |

Note. $q_m$, Dubinin–Radushkevich characteristic sorption capacity; beta, activity coefficient related to mean sorption energy; and $R^2$, coefficient of determination. BM, date palm leaf biomass; BC, biochar; OBC, ozonized biochar; NBC, nutrient-doped biochar; NOBC, nutrient-doped ozonized biochar; CD, carbon dots; OCD, ozonized carbon dots; NCD, nutrient-doped carbon dots; NOCD, nutrient-doped ozonized carbon dots.

*3.2.4. Kinetic Sorption*

Uptake followed three distinct kinetic phases for all four metals in the multi-metal solution (Fig. 6): an initial rapid phase within 50–150 min corresponding to surface adsorption on readily available sites; a slower phase between 100 and 200 min governed by intraparticle diffusion and progressive site saturation; and a plateau beyond 200 min indicating that equilibrium had been reached.

The pseudo-second-order (Fig. 7), Elovich (Fig. S4), intraparticle diffusion (Fig. S5) and power function (Fig. S6) models described the kinetic data well.

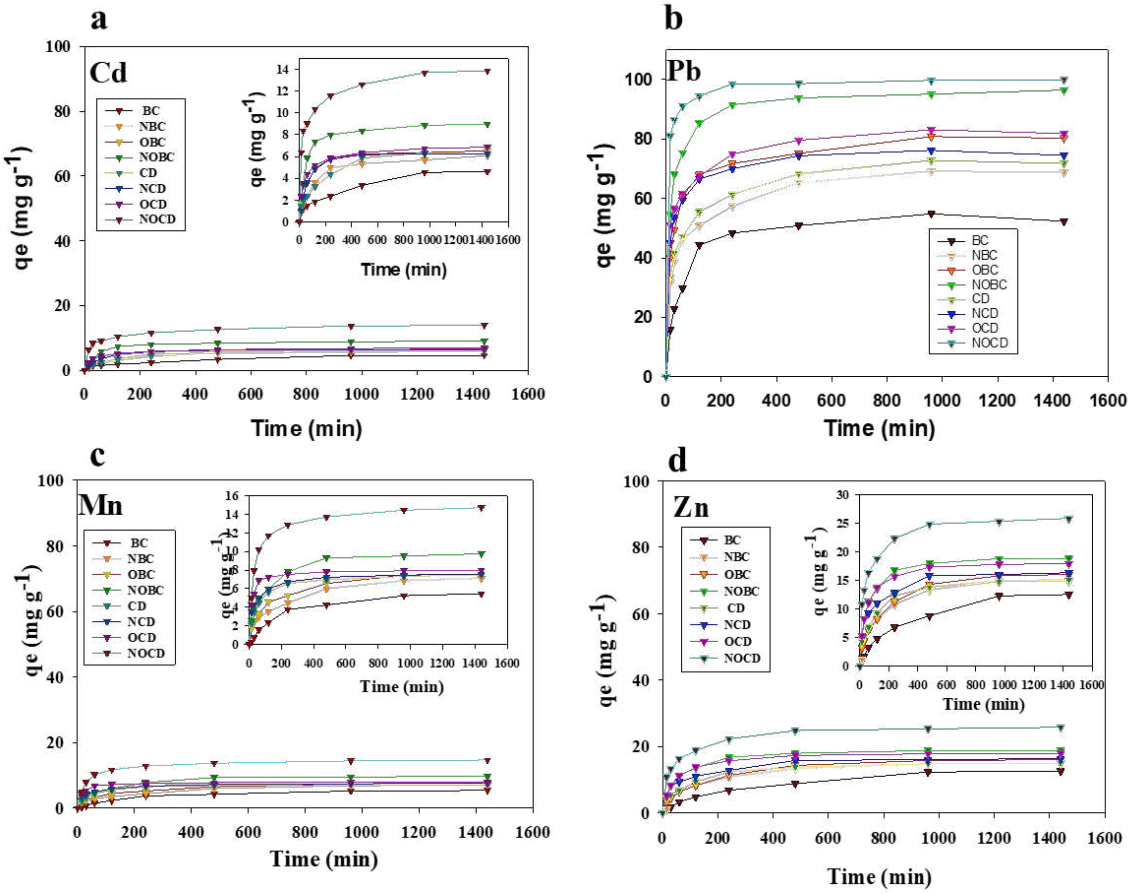



**Fig. 6** Effect of contact time on the competitive sorption of (a) $Cd^{2+}$, (b) $Pb^{2+}$, (c) $Mn^{2+}$ and (d) $Zn^{2+}$ from a multi-metal solution onto biochar (BC), ozonized biochar (OBC), nutrient-doped biochar (NBC), nutrient-doped ozonized biochar (NOBC), carbon dots (CD), ozonized carbon dots (OCD), nutrient-doped carbon dots (NCD) and nutrient-doped ozonized carbon dots (NOCD).

The pseudo-second-order was the best fitted model to explain sorption of the tested heavy metals onto synthesized materials (Table 6). NOCD exhibited the highest equilibrium capacity and the fastest initial uptake of $Cd^{2+}$ among all adsorbents (Table S3). The pseudo-second-order model returned $Q_e$ of 13.49 mg $g^{-1}$ and h of 0.28 mg $g^{-1}$ $min^{-1}$ for NOCD and Elovich α was likewise highest at 1.66 mg $g^{-1}$ $min^{-1,}$ as were

$k_{id}$, though NOBC's power-function $K_f$ (0.32 mg $g^{-1}$ $min^{-1}$) marginally exceeded NOCD's (0.31 mg $g^{-1}$ $min^{-1}$).

$Mn^{2+}$ uptake followed the same pattern and was well described by the pseudo-second-order model, with $R^2$ values of 0.97–0.99 (Table S4). NOCD again reached the highest $Q_e$ at 14.91 mg $g^{-1}$, although OCD recorded the fastest initial sorption rate (h = 0.70 mg $g^{-1}$ $min^{-1,}$), well above NOCD's 0.55 mg $g^{-1}$ $min^{-1}$, while intraparticle diffusion contributed to but did not limit the overall rate.

$Pb^{2+}$ showed the largest kinetic advantage for the NOCD of any metal studied (Table S5). The pseudo-second-order model again provided the best fit, with NOCD reaching $Q_e$ of 109.94 mg $g^{-1}$, approximately 4- to 8-fold above the equilibrium capacities (Qe) recorded for the other metals, and h of 7.96 mg $g^{-1}$ $min^{-1,}$, 9- to 28-fold above the initial sorption rates (h) recorded for the other metals; the Elovich model returned correspondingly higher α and β for NOCD.

$Zn^{2+}$ followed the same kinetic pattern as that of the other metals (Table S6). NOCD recorded the highest $Q_e$, h, Elovich α and Kid values of 26.19 mg $g^{-1}$, 0.91 mg $g^{-1}$ $min^{-1,}$ 13.22 mg $g^{-1}$ $min^{-1}$ and 1.71 mg $g^{-1}$ $min^{-1}$, respectively. For all four metals, higher initial concentrations accelerated the uptake and shortened the time to equilibrium, particularly for $Pb^{2+}$ and $Zn^{2+}$.

**Table 6** Pseudo-second order model parameters for the competitive sorption of the tested heavy metals from a multi-metal solution onto the synthesized carbon materials.

| Kinetic Models | Parameters | BC | NBC | OBC | NOBC | CD | NCD | OCD | NOCD |
|---|---|---|---|---|---|---|---|---|---|
| $Cd^{2+}$ | $k_2$ | $1.58 \times 10^{-3}$ | $2.10 \times 10^{-3}$ | $3.97 \times 10^{-3}$ | $3.25 \times 10^{-3}$ | $2.02 \times 10^{-3}$ | $3.91 \times 10^{-3}$ | $4.61 \times 10^{-3}$ | $1.53 \times 10^{-3}$ |
| | $Q_e$ | 4.93 | 6.30 | 6.66 | 9.15 | 6.61 | 6.45 | 6.96 | 13.49 |
| | h (mg $g^{-1}$ $min^{-1}$) | 0.04 | 0.08 | 0.18 | 0.27 | 0.09 | 0.16 | 0.22 | 0.28 |
| | $R^2$ | 0.97 | 0.99 | 0.99 | 0.99 | 0.99 | 0.99 | 0.99 | 0.99 |
| $Mn^{2+}$ | $k_2$ | $8.66 \times 10^{-4}$ | $1.73 \times 10^{-3}$ | $1.80 \times 10^{-3}$ | $2.00 \times 10^{-3}$ | $3.88 \times 10^{-3}$ | $5.38 \times 10^{-3}$ | $1.08 \times 10^{-2}$ | $2.48 \times 10^{-3}$ |
| | $Q_e$ | 6.17 | 7.36 | 7.90 | 10.00 | 7.61 | 7.67 | 8.04 | 14.91 |
| | h (mg $g^{-1}$ $min^{-1}$) | 0.03 | 0.09 | 0.11 | 0.20 | 0.22 | 0.32 | 0.70 | 0.55 |
| | $R^2$ | 0.97 | 0.99 | 0.99 | 0.99 | 0.99 | 0.99 | 0.99 | 0.99 |
| $Pb^{2+}$ | $k_2$ | $5.14 \times 10^{-4}$ | $4.90 \times 10^{-4}$ | $5.99 \times 10^{-4}$ | $8.24 \times 10^{-4}$ | $4.87 \times 10^{-4}$ | $9.54 \times 10^{-4}$ | $6.77 \times 10^{-4}$ | $6.60 \times 10^{-4}$ |
| | $Q_e$ | 55.46 | 70.49 | 81.62 | 96.92 | 73.85 | 76.44 | 83.69 | 109.94 |
| | h (mg $g^{-1}$ $min^{-1}$) | 1.58 | 2.43 | 3.99 | 7.74 | 2.66 | 5.57 | 4.74 | 7.96 |
| | $R^2$ | 0.99 | 0.99 | 0.99 | 0.99 | 0.99 | 0.99 | 0.99 | 0.99 |
| $Zn^{2+}$ | $k_2$ | $4.09 \times 10^{-4}$ | $6.53 \times 10^{-4}$ | $7.45 \times 10^{-4}$ | $1.47 \times 10^{-3}$ | $1.22 \times 10^{-3}$ | $1.55 \times 10^{-3}$ | $1.77 \times 10^{-3}$ | $1.33 \times 10^{-3}$ |
| | $Q_e$ | 13.91 | 15.94 | 16.87 | 19.32 | 15.53 | 16.72 | 18.31 | 26.19 |
| | h (mg $g^{-1}$ $min^{-1}$) | 0.08 | 0.17 | 0.21 | 0.55 | 0.30 | 0.43 | 0.59 | 0.91 |
| | $R^2$ | 0.97 | 0.99 | 0.99 | 0.99 | 0.99 | 0.99 | 0.99 | 0.99 |

Note. $k_2$, pseudo-second-order rate constant; $Q_e$, equilibrium sorption capacity; h, initial sorption rate; $R^2$, coefficient of determination. BM, date palm leaf biomass; BC, biochar; OBC, ozonized biochar; NBC, nutrient-doped biochar; NOBC, nutrient-doped ozonized biochar; CD, carbon dots; OCD, ozonized carbon dots; NCD, nutrient-doped carbon dots; NOCD, nutrient-doped ozonized carbon dots.

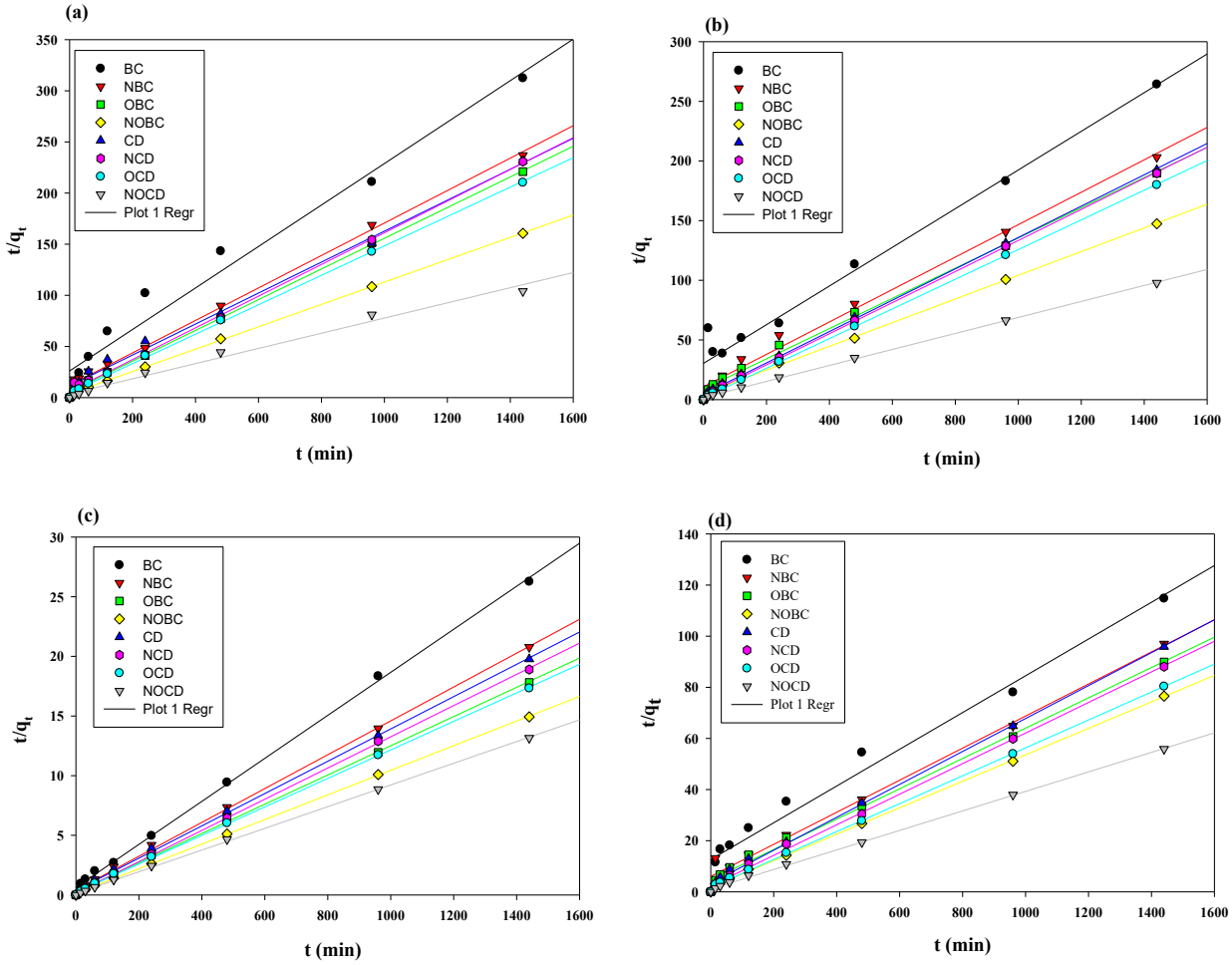



**Fig. 7** Pseudo-second-order kinetic fitting curves for the competitive sorption of (a) $Cd^{2+}$, (b) $Mn^{2+}$, (c) $Pb^{2+}$ and (d) $Zn^{2+}$ from a multi-metal solution onto biochar (BC), ozonized biochar (OBC), nutrient-doped biochar (NBC), nutrient-doped ozonized biochar (NOBC), carbon dots (CD), ozonized carbon dots (OCD), nutrient-doped carbon dots (NCD) and nutrient-doped ozonized carbon dots (NOCD).

## 4. Discussion

Heavy metal contamination of aquatic systems has proven to be one of the few environmental problems that grows rather than dissipates with time, because mining, smelting, electroplating and untreated industrial discharge deliver Pb, Cd, Mn and Zn to water bodies in forms that are neither degraded nor detoxified, so that each successive input is added to a standing inventory rather than replacing it (World Health Organization, 2008; Ali et al., 2019). This permanence is what translates modest aqueous concentrations into nephrotoxic, neurotoxic and carcinogenic exposures once the metals have partitioned into sediments, crops and human tissue and it is why source control alone has never been sufficient (Rahman and Singh, 2019; Bolan et al., 2014). The treatment technologies capable of meeting this burden, chemical precipitation, coagulation, ion exchange and membrane filtration, were developed for centralized, capital-rich settings and they transfer poorly to the arid and semi-arid regions where mining-affected water is most common, both because of cost and because they generate a metal-bearing sludge that simply relocates the problem (Liu et al., 2018; Babel and Kurniawan, 2003). Biomass-derived carbons have therefore been advanced as

the pragmatic alternative (Wang et al., 2023; Tan et al., 2015), yet the central weakness of that proposition has remained unresolved: pyrolysis, the step that creates the carbon skeleton, simultaneously destroys the oxygen functionality that binds divalent cations, so higher-temperature chars are structurally superior but chemically impoverished (Uchimiya et al., 2011; Sizmur et al., 2017). Reconciling those two requirements within a single low-cost material was the problem this study addressed, using date palm leaf residue, a regionally abundant waste that is burnt or landfilled and had not previously been examined in this role.

Progress on that reconciliation has been slowed less by a shortage of modification strategies than by the incommensurability of the evidence supporting them. Oxidative post-treatment, mineral or nutrient loading and hydrothermal conversion to nanoscale carbon have each been shown to improve metal uptake, but almost always on different feedstocks, at different pyrolysis temperatures and with different baselines. Therefore, the apparent superiority of any route cannot be separated from the conditions under which it was tested (Valdés et al., 2002; Ahmad et al., 2020; Kharel et al., 2019). Reviews of engineered biochars have repeatedly identified this fragmentation as the principal barrier to rational sorbent design and have called for factorial comparisons within a single system (Rajapaksha et al., 2016; Wang and Wang, 2019). The present study was designed to meet that requirement: one feedstock, one pyrolysis regime and one sorption protocol were held constant while ozonization, nutrient doping and carbon-dot conversion were varied factorially, so that the interaction between oxidative and nutrient functionalization could be measured rather than assumed. Resolving four metals simultaneously in a single multi-metal solution extended the comparison further, because competition for shared binding sites was then built into every measurement and selectivity, a property of both the material and the metal, cannot be inferred from single-metal studies. $Mn^{2+}$ is almost absent from the engineered biochar literature despite its prevalence in mine drainage (Park et al., 2016; Deng et al., 2019). The consequence of this design was not merely a better sorbent but a testable ranking of mechanisms and it is that ranking, rather than any individual capacity value, which the following sections interpret.

Pyrolysis and post-pyrolysis treatment act on entirely different property domains and recognizing that division is essential to interpreting everything that follows. The thermal step governs bulk chemistry: decarboxylation and dehydroxylation stripped the acidic functional groups that controlled the reaction pH of the raw leaf tissue, whereas alkali and alkaline-earth carbonates and oxides left behind in the ash imposed a strongly alkaline character on the char, shifting it from mildly acidic to pH 9.27 (Mukherjee et al., 2011; Tomczyk et al., 2020). Soluble salt behavior was governed by the same mass-balance logic in reverse: retention of salts in the solid phase raised conductivity in the pyrolyzed materials (Inyang et al., 2010), whereas hydrothermal processing partitioned those constituents into the aqueous phase and produced the least saline product of the series, an inadvertent desalting that Zhao et al. (2013) also observed when comparing feedstocks and production routes. Cation exchange capacity, by contrast, tracked the oxidative step almost exclusively, increasing 1.8-fold only where ozone had been applied. The mechanism is specific and well constrained: ozone attacks aromatic C=C bonds and abstracts aliphatic hydrogen to generate carboxylic, lactonic and phenolic groups that deprotonate in water to carboxylate and phenolate ligands, creating permanent negative charge where pyrolysis had removed it (Huff et al., 2018; Kharel et al., 2019; Munera-Echeverri et al., 2018). The untreated biomass, whose lignin-dominated matrix presents few accessible oxygenated ligands, defined the lower bound of exchange capacity and confirmed that the property is conferred by surface oxidation rather than inherited from the feedstock (Lehmann et al., 2011; Zhang et al., 2015).

If the oxidative step supplied reactivity, the thermal step supplied durability and the proximate data record that trade-off directly. The near-complete loss of volatile matter and the almost tenfold enrichment in fixed carbon documented the volatilization of cellulose and hemicellulose and the condensation of the surviving skeleton into aromatic domains, a transformation that determines not how much metal a char binds but how long it persists while binding it (Gai et al., 2014; Xiao et al., 2018). Aromatic condensation of this degree has been consistently associated with mean residence times of decades to centuries, whereas the parent biomass would be mineralized within a single season; therefore, the engineered materials acquired the environmental longevity that any practical sorbent or soil amendment requires (Lian and Xing, 2017). Ash rose sharply with pyrolysis itself rather than preferentially with doping, since added mineral salts are superimposed on inorganic residues already concentrated by pyrolysis; the significance is that this ash fraction is not inert filler but the source of the exchangeable counter-ions and precipitation nuclei invoked later to explain metal removal (Sun et al., 2014; Hossain et al., 2020). Moisture content, though low throughout, carried a comparable diagnostic weight: the driest material was the untreated char and the wettest the ozonized carbon dots, which showed that ozone had restored the surface hydrophilicity that high-temperature pyrolysis removed, a prerequisite for aqueous-phase accessibility of the newly created binding sites (Gale et al., 2021).

Nutrient fate was dictated by element volatility rather than treatment intensity and the three macronutrients accordingly diverged sharply. Nitrogen was lost almost entirely during pyrolysis, falling by two orders of magnitude as amide and amino functionality was thermally cleaved and the element was volatilized as NH3, HCN and N2 above 400 °C, a behavior that is now well established across feedstocks and temperature ranges (Ahmad et al., 2014; Zhang et al., 2020). Doping recovered only a fraction of this loss and the incompleteness of the recovery is informative: it implies that the applied nitrogen was retained largely as physically held or weakly sorbed species rather than being incorporated into the aromatic network, which limits both its agronomic persistence and its contribution to metal coordination (Ahmad et al., 2023; Dietrich et al., 2020). Phosphorus and potassium followed the opposite trajectory because neither is appreciably volatile at 400 to 600 °C; therefore, both were concentrated in the ash by the same mass loss that destroyed nitrogen and doping then raised phosphorus to nearly five times the feedstock concentration. This enrichment matters for two separate reasons: phosphate-loaded chars have repeatedly functioned as slow-release fertilizers (Yao et al., 2013; Lustosa Filho and Barbosa, 2019) and the accompanying soluble mineral load supplies the exchangeable cations whose displacement was later inferred from the sorption energetics (Gwenzi et al., 2018).

Infrared spectroscopy furnished decisive evidence that the treatments modified the surface chemistry independently of the bulk structure and the sequence of band changes read as a coherent account of loss followed by deliberate restoration. The disappearance of the broad hydroxyl envelope after pyrolysis confirmed the dehydration and dehydroxylation of cellulosic and phenolic hydroxyls and thereby located the origin of the exchange-capacity deficit that the thermal step imposed (Tomczyk et al., 2020; Ahmad et al., 2019a). The persistence of aromatic C=C absorption alongside the progressive weakening of aliphatic C–H and carboxylate features showed that condensation had advanced further than the retention of polar functionality, which is precisely the chemical condition under which a structurally mature char binds metals poorly (Xie et al., 2021; Kumar et al., 2023). Against that background, the behavior of the 1030 to 1100 $cm^{-1}$ region was diagnostic: these C–O–C, C–O and Si–O vibrations were absent from both the biomass and the untreated char yet prominent in every ozonized or doped product, demonstrating that oxygenated and silicate functionality was reinstated by the post-treatments and could not have arisen from pyrolysis (Chen et al.,

2017; Yang et al., 2019). Read together with the weak aromatic C–H bending observed across the treated series, the spectra described a surface that combined high aromaticity with restored polarity, a combination that the sorption data subsequently confirmed to be the optimal configuration for cation binding (Silos-Llamas et al., 2020; Kookana et al., 2011).

Diffraction resolved the question of where the inorganic phases identified spectroscopically actually resided and the answer was that they crystallized as discrete domains rather than remaining dispersed. The transition from the featureless hump of native lignocellulose to the weakly ordered pattern of the char marked incipient carbonization without crystalline development, confirming that pyrolysis at moderate temperatures organizes carbon only locally (Manya, 2012). The emergence of sharp quartz, calcite, iron and manganese oxide reflections in the ozonized and doped materials established that these phases either crystallized from inherent inorganic constituents or precipitated from the doping solution. This is mechanistically important because discrete mineral surfaces support precipitation and coprecipitation pathways that are unavailable to a purely organic sorbent (Zhang et al., 2025; Igalavithana et al., 2017). Within the carbon dot series, the broad reflection attributable to the (002) plane of turbostratic graphitic carbon indicated short-range stacking of aromatic layers and its retention alongside new crystalline reflections in the dual-treated material was the key observation: mineral growth did not consume the disordered carbon framework (Xiao et al., 2018). This coexistence explains why the most crystalline materials were also the best sorbents, as the mineral domains contributed structural stability and precipitation sites, while the residual amorphous regions retained the defect-rich, chemically reactive surface on which complexation depends (Wang and Wang, 2019; Zhu et al., 2020).

The textural data delivered the study's most counterintuitive result and, in doing so, overturned a common assumption about sorbent design. Pyrolysis behaved as expected, increasing the surface area twelvefold as volatilization opened micropore and small-mesopore networks along former cell-wall channels, so that the char and carbon dots represented the textural optimum of the series (Gale et al., 2021; Ahmad et al., 2019b). Every subsequent treatment then degraded that texture, with nutrient doping the most damaging and the carbon dot series the most severely affected, reduced to roughly one-quarter of its unmodified surface area. Two concurrent mechanisms account for the penalty: oxidative etching by ozone widens pore mouths and collapses thin pore walls, while precipitated nutrient salts occlude micropore entrances and both restrict nitrogen accessibility during analysis (Yuan et al., 2022; Sizmur et al., 2017; Xu et al., 2013). The critical point is that the sorption performance improved monotonically as the surface area declined. This inverse relationship demonstrates that chemical site density, not physical porosity, governs uptake in this system and it implies that BET area, still routinely reported as a proxy for sorbent quality, is actively misleading for cationic metals bound by specific surface chemistry, a conclusion reached independently for oxidized and mineral-loaded chars (Li and Dong, 2017; Peng et al., 2017).

Microscopy supplied physical corroboration for this interpretation by showing where the new chemistry was located. The progression from the smooth, semi-ordered surface of intact lignocellulose to the roughened, carbon-enriched char recorded devolatilization and aromatization, while ozonization produced a visibly more oxidized and etched texture consistent with the spectroscopic evidence of surface oxidation (Eldeeb et al., 2024; Zhou et al., 2017). Nutrient doping generated a distinctly heterogeneous surface carrying detectable nutrient elements in the energy-dispersive spectra, which established that dopants were deposited as discrete surface phases rather than distributed through the matrix and this localization explains both the porosity penalty and the availability of those phases as binding sites (Shi et al., 2019; Sun et al., 2020). The carbon dot series was informative in a different way, since the treatments altered particle

organization rather than surface relief alone: uniform spheres in the unmodified material became most dispersed after ozonization, most compact after doping and most irregular when both were applied. Electrostatic repulsion between surface carboxylates accounts for the dispersion, whereas nucleation of mineral precipitates on an already oxidized surface accounts for the irregularity of the dual-treated product; therefore, the morphology of the best-performing material was itself the visible signature of the two mechanisms acting in sequence (Zhou et al., 2018; Li et al., 2021).

Solution pH emerged as the dominant control on removal and the shape of the response was itself mechanistic rather than merely an operating datum. The uptake of all four metals increased with pH to a maximum at pH 5 and declined thereafter, a curve that can only be produced by surface sites whose charge is pH-dependent: below pH 5, the carboxyl and hydroxyl groups remained protonated, the surface carried a net positive charge and protons outcompeted metal cations for the few available ligands (Mohan and Pittman Jr, 2007; Bentahar et al., 2016). Progressive deprotonation toward pH 5 converted repulsion into attraction and permitted inner-sphere complexation, whereas the decline above pH 5 reflected hydroxide and carbonate precipitation, together with the formation of hydrolyzed species such as PbOH+ that coordinate less readily to anionic sites; therefore, the apparent optimum marked the boundary between adsorption and bulk precipitation rather than a maximum in surface affinity (Lu et al., 2012; Wang et al., 2015). More revealing than the optimum was the invariance of its position across all eight materials, which indicated that the treatments multiplied the number of binding sites without altering their chemical identity. Metal-specific behavior followed the same logic: $Pb^{2+}$ was removed most efficiently on every sorbent because its large ionic radius, low hydration energy, high electronegativity and strong first hydrolysis tendency favor dehydration and direct coordination (Cao et al., 2009; Trakal et al., 2014), $Cd^{2+}$ tracked the identical sorbent ranking on a far lower plateau because its higher hydration energy resists the ligand exchange that binding requires (Xu et al., 2013; Cui et al., 2016) and $Mn^{2+}$ remained nearly pH-insensitive, consistent with an ion that stays fully hydrated and interacts only weakly and outer-spherically, with $Zn^{2+}$ intermediate between these extremes (Ahmad et al., 2014; Chen et al., 2011).

The dose response identified 1.0 g $L^{-1}$ as the operational optimum and, failing to improve beyond it, exposed a mass-transfer rather than a chemical constraint. Removal increased between 0.5 and 1.0 g $L^{-1}$ for the trivial reason that binding sites per unit volume increased, but the decline at 2.0 g $L^{-1}$ cannot be explained chemically, since adding sorbent cannot remove binding sites. Two physical processes account for this: particle aggregation and interparticle shielding reduce the externally accessible surface and lengthen intraparticle diffusion paths, while the solution concentration gradient becomes too shallow to sustain transfer once most of the metal has already been captured (Goel et al., 2005; Ebrahimi et al., 2013). Support for this interpretation came from the metal-specific pattern, because lead retained high removal even at the lowest loading, indicating a site affinity sufficiently high that sorbent mass was never the limiting factor, whereas the weakly bound metals responded more sharply to dose and were correspondingly more sensitive to aggregation. The practical implication is that over-dosing is not merely wasteful but counterproductive and the convergence of this optimum with the 1 to 2 g $L^{-1}$ window reported for oxidized and mineral-modified chars in multi-metal solutions suggests the constraint is a general property of fine carbonaceous sorbents rather than an artifact of this material (Park et al., 2016; Kilic et al., 2013).

Equilibrium modeling explained why combining the two treatments outperformed either treatment alone, which was the central question the factorial design was built to answer. The plateau in uptake with increasing initial concentration confirmed that site availability, not solution supply, became limiting as equilibrium was approached (Foo and Hameed, 2010). The resulting competitive affinity sequence of $Pb^{2+} > Zn^{2+} >$

$Cd^{2+}$ > $Mn^{2+}$ in the multi-metal solution reproduced the order of electronegativity and hydrolysis tendency, which is the signature of specific chemical adsorption rather than electrostatic accumulation (Xu et al., 2014; Zama et al., 2017). The fact that the Langmuir model best described lead sorption, while Freundlich fits remained acceptable for all four metals, is not a contradiction but a description of a compositionally mixed surface, on which a set of high-affinity, energetically comparable sites coexists with a broader heterogeneous population, exactly as expected where organic and mineral binding domains occupy the same particle (Mohan et al., 2011; Li and Dong, 2017). Freundlich exponents below unity for all materials confirmed energetically favorable adsorption onto such a heterogeneous surface (Okpara et al., 2021; Keerthanan et al., 2020). The decisive observation was additive rather than absolute: ozonization alone and doping alone each substantially raised the monolayer lead capacity and their combination raised it further, to 138.31 mg $g^{-1,}$ which established that the two treatments furnished chemically distinct and non-competing site types, oxidation supplying deprotonatable oxygen ligands and doping supplying exchangeable mineral counter-ions together with precipitation nuclei (Peng et al., 2017; Xue et al., 2012).

diffraction data have already shown to be chemically heterogeneous and goodness of fit therefore carried no interpretive weight; the model was accordingly excluded from the sorbent ranking (Foo and Hameed, 2010). In contrast, the Dubinin-Radushkevich model independently reproduced the Langmuir ranking for every metal and this agreement between the two models, resting on different assumptions, provided the strongest available evidence that the ranking reflected a real property of the materials rather than a fitting artifact. Its principal contribution was energetic: the narrow range of activity coefficients corresponded to mean sorption energies above 8 kJ $mol^{-1,}$ placing the process in the chemisorption domain with a supporting ion-exchange component and excluding physical pore filling as a significant pathway, a conclusion consistent with the observation that uptake increased as porosity decreased (Ho et al., 2002; Reddy and Lee, 2014).

Kinetic behavior was uniform across all four metals, and this uniformity was itself diagnostic of a shared binding mechanism operating at different intensities. Three phases were resolved in every system: an initial rapid stage as accessible external sites were occupied, a slower interval governed by intraparticle diffusion and progressive saturation and a plateau at equilibrium, which is the canonical profile of a chemically heterogeneous porous sorbent. Pseudo-second-order kinetics best described the data throughout, indicating that the rate-limiting step involved valence forces through electron sharing or exchange between metal cations and surface functional groups rather than film diffusion and thereby corroborating the chemisorption energetics derived independently from the equilibrium data (Ho and Mc, 1999). The dual-treated material combined the highest equilibrium capacity with the fastest initial rate for every metal, a combination that is not self-evident, since higher capacity is frequently accompanied by slower approach to equilibrium when uptake depends on diffusion into constricted pores; its absence here reinforces the conclusion that binding occurred predominantly at accessible surface sites. Elovich parameters rose in the same order and the desorption constant for lead was the highest of the series, signaling strong chemisorption and marked resistance to release, which is the property that determines whether a spent sorbent can be disposed of safely (Silos-Llamas et al., 2020; Wang et al., 2022). Intraparticle diffusion nonetheless contributed to the overall rate without controlling it, since the fitted lines did not pass through the origin and the boundary-layer term increased systematically with treatment intensity, consistent with surface modification thickening the diffusional film (Weber and Morris, 1963), while the acceleration of uptake at higher initial concentrations followed directly from the steeper gradient across that film (Mahdi et al., 2018).

As all the measurements were conducted in a multi-metal solution, the affinity sequence for the metals $Pb^{2+}$ > $Zn^{2+}$ > $Cd^{2+}$ > $Mn^{2+}$ on NOCD was a competitive sequence. $Pb^{2+}$, due to its low hydration energy, high electronegativity and a tendency to form sparingly soluble phosphate and carbonate phases, could occupy the strongest sites first, which resulted in 97% removal of $Pb^{2+}$, compared to only 4% to 20% of $Cd^{2+}$, $Mn^{2+}$ and $Zn^{2+}$ at the same initial concentration. Overall, NOCD was the best sorbent for $Pb^{2+}$-selective removal. Assembled into a single account, the characterization and sorption evidence converge on four mechanisms acting in parallel and the value of the factorial design lies in the fact that each can be attached to a specific observation rather than assumed. Complexation by ozone-generated carboxyl, lactonic, hydroxyl and carbonyl ligands was evidenced by the restored infrared bands and the increase in exchange capacity; electrostatic attraction to deprotonated sites by the invariant pH 5 optimum; cation exchange with doping-derived mineral counter-ions by the Dubinin-Radushkevich energies together with the elevated ash and potassium contents; and surface precipitation or coprecipitation with carbonate, phosphate and oxide phases by the crystalline reflections confined to the doped materials, a pathway of particular importance for $Pb^{2+}$ given the extreme insolubility of its hydroxypyromorphite and cerussite analogs (Zhu et al., 2020; Lu et al., 2012; Cao et al., 2009). Cation-pi coordination with the graphitic domains detected by diffraction cannot be excluded and has been invoked for lead on aromatic-rich chars, though the present data cannot isolate its contribution (Xiao et al., 2018; Yang et al., 2019). Two broader conclusions follow. First, because lead capacity increased by a factor of 2.4 while the surface area fell to one quarter of its maximum, surface chemistry can be engineered independently of texture, and porosity metrics should not be used to screen sorbents intended for cationic metals. Second, a single material captured four co-occurring metals from one multi-metal solution, in competition with one another and with retention energies indicative of chemisorption, which is the operationally relevant result, since mining-impacted and industrial effluents are invariably multi-metal and sequential single-metal treatment is rarely affordable (Mohanty et al., 2018; Palansooriya et al., 2020).

4.1. Cost-effectiveness

Laboratory performance is a necessary but insufficient condition for deployment and the modification sequence examined here was therefore assessed against the cost structure of the incumbent technology. Granular activated carbon derives most of its expense from activation at 800 to 1000 °C with steam or chemical agents, whereas slow pyrolysis of agricultural residue at 400 to 600 °C has been costed at roughly one-third to one-tenth of that figure, a margin attributable principally to lower energy demand and to feedstock that carries a negative acquisition cost where its disposal is otherwise a liability (Roberts et al., 2010; Alhashimi and Aktas, 2017). Life-cycle comparisons have shown that the advantage is environmental as well as financial, with biochar-based tertiary treatment achieving substantially lower global warming potential and cumulative energy demand for equivalent contaminant removal and the margin widening when production occurs in the region where the residue arises (Thompson et al., 2016). Against that baseline, ozonization is unusually well suited to decentralized operation because ozone is generated electrically from ambient air or oxygen and consumed in situ, so no chemical inventory is held, no spent regenerant is produced and, unlike the nitric acid, permanganate, or peroxide routes conventionally used to oxidize chars, no acidic or metal-bearing effluent requires neutralization and disposal (Huff et al., 2018; Eldeeb et al., 2024). Nutrient doping relies on commodity fertilizer salts already traded at an agricultural scale and the phosphorus and potassium enrichment it confers means that a spent sorbent which has not accumulated regulated metal loads retains residual agronomic value, which converts an end-of-life cost into partial cost recovery (Gwenzi et al., 2018; Vikrant et al., 2018).

4.2. Implications of the Study

These findings have practical implications for the design of low-cost water treatment materials in regions where mining or industrial activity has degraded local water quality. Because NOCD is derived entirely from an agricultural by-product (date palm leaves) using ozone gas and low-cost nutrient salts rather than hazardous acids or bases, its production pathway is compatible with decentralized, small-scale manufacture in date palm-producing regions of the Middle East and North Africa, where feedstock is abundant and disposal of palm residues is itself a waste-management challenge. The simultaneous removal of four co-occurring metals by a single material under competitive conditions also has direct relevance for treating real mining-impacted or industrial effluents, which rarely contain only one contaminant and reduces the need for multiple metal-specific adsorbents or sequential treatment stages.

## 5. Conclusions

Pyrolysis converts lignocellulosic waste into porous carbon; however, simultaneously destroys much of the oxygen functionality on which cation binding depends, a trade-off that limits the direct use of pyrolyzed carbons as sorbents for treating $Pb^{2+}$, $Cd^{2+}$, $Mn^{2+}$ and $Zn^{2+}$ in water. This study converted date palm leaf residue, a regionally abundant waste that is routinely burnt or landfilled, into eight engineered carbon sorbents and determined whether ozonization and nutrient doping, applied singly and in combination to biochar and to its hydrothermally derived carbon dots, could restore the functionality lost during pyrolysis. This comparison was necessary because these two post-pyrolysis modification routes had never been evaluated within one feedstock and sorption system. Carbonization increased fixed carbon and surface area, whereas ozonization and doping restored carboxyl, phenolic and mineral binding sites and increased cation exchange capacity despite lowering porosity. Removal peaked at pH 5 and a sorbent dose of 1.0 g $L^{-1}$ and the nutrient-doped ozonized carbon dots surpassed all other materials, attaining a Langmuir lead capacity of 138.31 mg $g^{-1}$ in the multi-metal solution, with a competitive affinity sequence of $Pb^{2+}$, $Zn^{2+}$, $Cd^{2+}$ and $Mn^{2+}$; Langmuir and pseudo-second-order fits indicated monolayer chemisorption via complexation, cation exchange and surface precipitation on functionalized surfaces. Uptake increased as surface area decreased, establishing surface chemistry rather than porosity as the operative design variable for pyrolysis-derived sorbents. Under competition, $Pb^{2+}$ remained the dominant metal on every material, yet NOCD increased the Langmuir capacity for all four metals by 50% to 158%, indicating that the treatments increased site density without displacing this order; removal of $Cd^{2+}$, $Mn^{2+}$ and $Zn^{2+}$ nevertheless stayed low (4% to 20% at pH 5) in the presence of $Pb^{2+}$. Combined post-pyrolysis surface engineering thus offers a scalable route to convert an agricultural waste pyrolysis product into an efficient sorbent for treating contaminated water.

## CRediT Authorship Contribution Statement

All authors contributed to the study conception and design. M.U. contributed in conceptualization, investigation, methodology, conducting sorption batch trials, analyses, and writing the original draft. M.A. contributed in conceptualization, investigation, methodology, supersizing the experimentation, and writing and reviewing the manuscript. M.I.A. contributed in conceptualization, supervising the experimentation, resource management, and writing and reviewing the manuscript. J.A. contributed in analyses, data curation and interpretation of data. M.I.R. contributed in data curation, methodology, and writing and reviewing the manuscript. H.A.A. contributed in methodology, data interpretation, and writing and reviewing the manuscript. A.S.A. contributed in project administration, and reviewing the manuscript. All authors reviewed the manuscript and approved it for publication.

## Declaration of Competing Interest

The authors declare that they have no known competing financial interests or personal relationships that could have influenced the work reported in this paper.

## Data Availability Statement

Data supporting the findings of this study are available from the corresponding author upon reasonable request.

## References


Ahmad, M., Moon, D.H., Vithanage, M., Koutsospyros, A., Lee, S.S., & Yang, J.E. (2014). Production and use of biochar from buffalo-weed (Ambrosia trifida L.) for trichloroethylene removal from water, *J. Chem. Technol. Biotechnol. 89 (2014) 150-157.*.

Ahmad, M., Ahmad, M., Usman, A.R., Al-Faraj, A.S., Abduljabbar, A., Ok, Y.S., & Al-Wabel, M.I. (2019a). Date palm waste-derived biochar composites with silica and zeolite: synthesis, characterization and implication for carbon stability and recalcitrant potential, *Environ. Geochem. Health 41 (2019)* 1687-1704.

Ahmad, M., Usman, A.R., Rafique, M.I., & Al-Wabel, M.I. (2019b). Engineered biochar composites with zeolite, silica and nano-zerovalent iron for the efficient scavenging of chlortetracycline from aqueous solutions, *Environ. Sci. Pollut. Res. 26 (2019)* 15136-15152.

Ahmad, M., Akanji, M.A., Usman, A.R., Al-Farraj, A.S., Tsang, Y.F., & Al-Wabel, M.I. (2020). Turning date palm waste into carbon nanodots and nano zerovalent iron composites for excellent removal of methylthioninium chloride from water, *Sci. Rep. 10 (2020)* 16125.

Ahmad, S., Liu, L., Zhang, S., & Tang, J. (2023). Nitrogen-doped biochar (N-doped BC) and iron/nitrogen co-doped biochar (Fe/N co-doped BC) for removal of refractory organic pollutants, *J. Hazard. Mater. 446 (2023)* 130727.

Alhashimi, H.A., & Aktas, C.B. (2017). Life cycle environmental and economic performance of biochar compared with activated carbon: A meta-analysis, *Resour. Conserv. Recycl. 118 (2017)* 13-26.

Ali, H., Khan, E., & Ilahi, I. (2019). Environmental chemistry and ecotoxicology of hazardous heavy metals: Environmental persistence, toxicity and bioaccumulation, *J. Chem. 2019 (2019)* 6730305.

An, X., Yu, J., Yu, J., Tahmasebi, A., Wu, Z., Liu, X., & Yu, B. (2020). Incorporation of biochar into semi-interpenetrating polymer networks through graft co-polymerization for the synthesis of new slow-release fertilizers, *J. Clean. Prod. 272 (2020)* 122731.

ASTM International (1989). *Standard Test Method for Chemical Analysis of Wood Charcoal* (ASTM D1762-84), ASTM International, West Conshohocken, PA.

Babel, S., & Kurniawan, T.A. (2003). Low-cost adsorbents for heavy metals uptake from contaminated water: a review, *J. Hazard. Mater. 97 (2003)* 219-243.

Banerjee, P., & Prasad, B. (2020). Determination of concentration of total sodium and potassium in surface and ground water using a flame photometer, *Appl. Water Sci. 10* (2020) 1-7.

Bentahar, Y., Hurel, C., Draoui, K., Khairoun, S., & Marmier, N. (2016). Adsorptive properties of Moroccan clays for the removal of arsenic (V) from aqueous solution, *Appl. Clay Sci. 119* (2016) 385-392.

Bolan, N., Kunhikrishnan, A., Thangarajan, R., Kumpiene, J., Park, J., Makino, T., Kirkham, M.B., & Scheckel, K. (2014). Remediation of heavy metal(loid)s contaminated soils: To mobilize or to immobilize?, *J. Hazard. Mater. 266 (2014)* 141-166.

Burezq, H., & Davidson, M.K. (2023). Biochar from date palm (Phoenix dactylifera L.) residues-a critical review, *Arab. J. Geosci. 16 (2023)* 101.

Cao, X., Ma, L., Gao, B., & Harris, W. (2009). Dairy-manure derived biochar effectively sorbs lead and atrazine, *Environ. Sci. Technol. 43 (2009)* 3285-3291.

Chen, X., Chen, G., Chen, L., Chen, Y., Lehmann, J., McBride, M.B., & Hay, A.G. (2011). Adsorption of copper and zinc by biochars produced from pyrolysis of hardwood and corn straw in aqueous solution, *Bioresour. Technol. 102* (2011) 8877-8884.

Chen, L., Chen, X.L., Zhou, C.H., Yang, H.M., Ji, S.F., & Tong, D.S. (2017). Environmental-friendly montmorillonite-biochar composites: Facile production and tunable adsorption-release of ammonium and phosphate, *J. Clean. Prod. 156 (2017)* 648-659.

Chen, Q., Cao, X., Li, Y., Sun, Q., Dai, L., & Li, J. (2022). Functional carbon nanodots improve soil quality and tomato tolerance in saline-alkali soils, *Sci. Total Environ. 830 (2022)* 154817.

Cui, X., Fang, S., Yao, Y., Li, T., Ni, Q., Yang, X., & He, Z. (2016). Potential mechanisms of cadmium removal from aqueous solution by Canna indica derived biochar, *Sci. Total Environ. 562* (2016) 517-525.

Deng, Y., Huang, S., Laird, D.A., Wang, X., & Meng, Z. (2019). Adsorption behavior and mechanisms of cadmium and nickel on rice straw biochars in single- and binary-metal systems, *Chemosphere 218* (2019) 308-318.

Dietrich, C.C., Rahaman, M.A., Robles-Aguilar, A.A., Latif, S., Intani, K., Müller, J., & Jablonowski, N.D. (2020). Nutrient loaded biochar doubled biomass production in juvenile maize plants (*Zea mays* L.), *Agronomy 10 (2020)* 567.

Ebrahimi, R., Maleki, A., Shahmoradi, B., Daraei, H., Mahvi, A.H., Barati, A.H., & Eslami, A. (2013). Elimination of arsenic contamination from water using chemically modified wheat straw, *Desalin. Water Treat. 51* (2013) 2306-2316.

Eldeeb, T.M., Aigbe, U.O., Ukhurebor, K.E., Onyancha, R.B., El-Nemr, M.A., & Hassaan, M.A. (2024). Adsorption of methylene blue (MB) dye on ozone, purified and sonicated sawdust biochars, *Biomass Convers. Biorefin. 14 (2024)* 9361-9383.

Foo, K.Y., & Hameed, B.H. (2010). Insights into the modeling of adsorption isotherm systems, *Chem. Eng. J. 156* (2010) 2-10.

Gai, X., Wang, H., Liu, J., Zhai, L., Liu, S., Ren, T., & Liu, H. (2014). Effects of feedstock and pyrolysis temperature on biochar adsorption of ammonium and nitrate, *PLoS One 9 (2014)* e113888.

Gale, M., Nguyen, T., Moreno, M., & Gilliard-Abdul, K.L. (2021). Aziz, Physiochemical properties of biochar and activated carbon from biomass residue: influence of process conditions to adsorbent properties, *ACS Omega 6* (2021) 10224-10233.

Goel, J., Kadirvelu, K., Rajagopal, C., & Garg, V.K. (2005). Removal of lead (II) by adsorption using treated granular activated carbon: batch and column studies, *J. Hazard. Mater. 125 (2005)* 211-220.

Gwenzi, W., Nyambishi, T.J., Chaukura, N., & Mapope, N. (2018). Synthesis and nutrient release patterns of a biochar-based N-P-K slow-release fertilizer, *Int. J. Environ. Sci. Technol. 15 (2018) 405-414.*.

Ho, Y.S., & McKay, G. (1999). Pseudo-second order model for sorption processes, *Process Biochem. 34* (1999) 451-465.

Ho, Y.S., Porter, J.F., & McKay, G. (2002). Equilibrium isotherm studies for the sorption of divalent metal ions onto peat: copper, nickel and lead single component systems, *Water Air Soil Pollut. 141* (2002) 1-33.

Hossain, M.Z., Bahar, M.M., Sarkar, B., Donne, S.W., Ok, Y.S., Palansooriya, K.N., Kirkham, M.B., Chowdhury, S., & Bolan, N. (2020). Biochar and its importance on nutrient dynamics in soil and plant, *Biochar 2* (2020) 379-420.

Hossner, L.R. (1996). Dissolution for total elemental analysis, *Methods Soil Anal. Part 3 5 (1996) 49-64.*.

Huff, M.D., Marshall, S., Saeed, H.A., & Lee, J.W. (2018). Surface oxygenation of biochar through ozonization for dramatically enhancing cation exchange capacity, *Bioresour. Bioprocess. 5 (2018)* 18.

Igalavithana, A.D., Mandal, S., Niazi, N.K., Vithanage, M., Parikh, S.J., Mukome, F.N.D., Rizwan, M., Oleszczuk, P., Al-Wabel, M., Bolan, N., Tsang, D.C.W., Kim, K.H., & Ok, Y.S. (2017). Advances and future directions of biochar characterization methods and applications, *Crit. Rev. Environ. Sci. Technol. 47 (2017) 2275-2330.*.

Inyang, M., Gao, B., Pullammanappallil, P., Ding, W., & Zimmerman, A.R. (2010). Biochar from anaerobically digested sugarcane bagasse, *Bioresour. Technol. 101* (2010) 8868-8872.

Kavitha, B., Reddy, P.V.L., Kim, B., Lee, S.S., Pandey, S.K., & Kim, K.H. (2018). Benefits and limitations of biochar amendment in agricultural soils: A review, *J. Environ. Manage. 227 (2018)* 146-154.

Keerthanan, S., Bhatnagar, A., Mahatantila, K., Jayasinghe, C., Ok, Y.S., & Vithanage, M. (2020). Engineered tea-waste biochar for the removal of caffeine, a model compound in pharmaceuticals and personal care products (PPCPs), from aqueous media, *Environ. Technol. Innov. 19 (2020)* 100847.

Kharel, G., Sacko, O., Feng, X., Morris, J.R., Phillips, C.L., Trippe, K., Kumar, S., & Lee, J.W. (2019). Biochar surface oxygenation by ozonization for super high cation exchange capacity, *ACS Sustain. Chem. Eng. 7 (2019)* 16410-16418.

Kilic, M., Kirbiyik, C., Cepeliogullar, O., & Putun, A.E. (2013). Adsorption of heavy metal ions from aqueous solutions by bio-char, a by-product of pyrolysis, *Appl. Surf. Sci. 283* (2013) 856-862.

Kookana, R.S., Sarmah, A.K., Van Zwieten, L., Krull, E., & Singh, B. (2011). Biochar application to soil: agronomic and environmental benefits and unintended consequences, *Adv. Agron. 112 (2011)* 103-143.

Kumar, S., Masto, R.E., & Kaushik, G. (2023). Thermally processed biochar: preparation, characterisation and their application for cadmium removal from surface and groundwater, *Int. J. Environ. Anal. Chem. 103 (2023)* 6539-6558.

Lehmann, J., Rillig, M.C., Thies, J., Masiello, C.A., Hockaday, W.C., & Crowley, D. (2011). Biochar effects on soil biota-a review, *Soil Biol. Biochem. 43 (2011)* 1812-1836.

Li, H., & Dong, X. (2017). E.B. da Silva, L.M. de Oliveira, Y. Chen, L.Q. Ma, Mechanisms of metal sorption by biochars: Biochar characteristics and modifications, *Chemosphere 178* (2017) 466-478.

Li, Y., Pan, X., Xu, X., Wu, Y., Zhuang, J., & Zhang, X. (2021). Carbon dots as light converter for plant photosynthesis: Augmenting light coverage and quantum yield effect, *J. Hazard. Mater. 410 (2021)* 124534.

Lian, F., & Xing, B. (2017). Black carbon (biochar) in water/soil environments: Molecular structure, sorption, stability and potential risk, *Environ. Sci. Technol. 51 (2017)* 13517-13532.

Liu, W., Tian, J., Chen, L., & Guo, Y. (2017). Temporal and spatial characteristics of lead emissions from the lead-acid battery manufacturing industry in China, *Environ. Pollut. 220* (2017) 696-703.

Liu, L., Li, W., Song, W., & Guo, M. (2018). Remediation techniques for heavy metal-contaminated soils: Principles and applicability, *Sci. Total Environ. 633* (2018) 206-219.

Lu, H., Zhang, W., Yang, Y., Huang, X., Wang, S., & Qiu, R. (2012). Relative distribution of Pb2+ sorption mechanisms by sludge-derived biochar, *Water Res. 46* (2012) 854-862.

Lustosa Filho, J.F., & Barbosa, C.F. (2019). J.S. da Silva Carneiro, L.C.A. Melo, Diffusion and phosphorus solubility of biochar-based fertilizer: Visualization, chemical assessment and availability to plants, *Soil Tillage Res. 194 (2019)* 104298.

Mahdi, Z., Yu, Q.J., & El Hanandeh, A. (2018). Removal of lead (II) from aqueous solution using date seed-derived biochar: batch and column studies, *Appl. Water Sci. 8 (2018)* 181.

Mahmoud, E.R.I., Aly, H.M., Hassan, N.A., Aljabri, A., Khan, A.L., & El-Labban, H.F. (2024). Biochar from date palm waste via two-step pyrolysis: A novel approach for Cu(II) removal from wastewater, *Processes 12 (2024)* 1189.

Manya, J.J. (2012). Pyrolysis for biochar purposes: A review to establish current knowledge gaps and research needs, *Environ. Sci. Technol. 46 (2012)* 7939-7954.

Mohan, D., & Pittman Jr, C.U. (2007). Arsenic removal from water/wastewater using adsorbents-a critical review, *J. Hazard. Mater. 142 (2007)* 1-53.

Mohan, D., Rajput, S., Singh, V.K., Steele, P.H., & Pittman Jr, C.U. (2011). Modeling and evaluation of chromium remediation from water using low cost bio-char, a green adsorbent, *J. Hazard. Mater. 188 (2011)* 319-333.

Mohanty, S.K., Valenca, R., Berger, A.W., Yu, I.K.M., Xiong, X., Saunders, T.M., & Tsang, D.C.W. (2018). Plenty of room for carbon on the ground: Potential applications of biochar for stormwater treatment, *Sci. Total Environ. 625* (2018) 1644-1658.

Mukherjee, A., Zimmerman, A.R., & Harris, W. (2011). Surface chemistry variations among a series of laboratory-produced biochars, *Geoderma 163* (2011) 247-255.

Munera-Echeverri, J.L., Martinsen, V., Strand, L.T., Zivanovic, V., Cornelissen, G., & Mulder, J. (2018). Cation exchange capacity of biochar: An urgent method modification, *Sci. Total Environ. 642* (2018) 190-197.

Okpara, O.G., Ogbeide, O.M., Ike, O.C., Menechukwu, K.C., & Ejike, E.C. (2021). Optimum isotherm by linear and nonlinear regression methods for lead (II) ions adsorption from aqueous solutions using synthesized coconut shell-activated carbon (SCSAC), *Toxin Rev. 40* (2021) 901-914.

Olsen, S.R., & Sommers, L.E. (1982). Phosphorus, in: A.L. Page (Ed.), *Methods of Soil Analysis: Part 2. Chemical and Microbiological Properties,* 2nd ed., American Society of Agronomy, Soil Science Society of America, Madison, WI, pp. 403-430.

Palansooriya, K.N., Yang, Y., Tsang, Y.F., Sarkar, B., Hou, D., Cao, X., Meers, E., Rinklebe, J., Kim, K.H., & Ok, Y.S. (2020). Occurrence of contaminants in drinking water sources and the potential of biochar for water quality improvement: A review, *Crit. Rev. Environ. Sci. Technol. 50 (2020) 549-611.*.

Park, J.H., Ok, Y.S., Kim, S.H., Cho, J.S., Heo, J.S., Delaune, R.D., & Seo, D.C. (2016). Competitive adsorption of heavy metals onto sesame straw biochar in aqueous solutions, *Chemosphere 142* (2016) 77-83.

Peng, H., Gao, P., Chu, G., Pan, B., Peng, J., & Xing, B. (2017). Enhanced adsorption of Cu(II) and Cd(II) by phosphoric acid-modified biochars, *Environ. Pollut. 229* (2017) 846-853.

Rahman, Z., & Singh, V.P. (2019). The relative impact of toxic heavy metals (THMs)(arsenic (As), cadmium (Cd), chromium (Cr)(VI), mercury (Hg) and lead (Pb)) on the total environment: an overview, *Environ. Monit. Assess. 191 (2019)* 419.

Rajapaksha, A.U., Chen, S.S., Tsang, D.C.W., Zhang, M., Vithanage, M., Mandal, S., Gao, B., Bolan, N.S., & Ok, Y.S. (2016). Engineered/designer biochar for contaminant removal/immobilization from soil and water: Potential and implication of biochar modification, *Chemosphere 148* (2016) 276-291.

Reddy, D.H.K., & Lee, S.M. (2014). Magnetic biochar composite: facile synthesis, characterization and application for heavy metal removal, *Colloids Surf. A 454 (2014) 96-103.*.

Roberts, K.G., Gloy, B.A., Joseph, S., Scott, N.R., & Lehmann, J. (2010). Life cycle assessment of biochar systems: Estimating the energetic, economic and climate change potential, *Environ. Sci. Technol. 44 (2010)* 827-833.

Shaban, M., Zhu, Y., Alharbi, N.S., Ren, X., & Chen, C. (2025). Enhanced U (VI) separation from aqueous solution with plasma-reduced nZV Fe/Ni doped biochar: Performance and mechanism, *Sep. Purif. Technol. 361 (2025)* 131404.

Shi, J., Fan, X., Tsang, D.C., Wang, F., Shen, Z., Hou, D., & Alessi, D.S. (2019). Removal of lead by rice husk biochars produced at different temperatures and implications for their environmental utilizations, *Chemosphere 235* (2019) 825-831.

Silos-Llamas, A.K., Durán-Jiménez, G., Hernández-Montoya, V., Montes-Morán, M.A., & Rangel-Vázquez, N.A. (2020). Understanding the adsorption of heavy metals on oxygen-rich biochars by using molecular simulation, *J. Mol. Liq. 298 (2020)* 112069.

Sizmur, T., Fresno, T., Akgul, G., Frost, H., & Moreno-Jimenez, E. (2017). Biochar modification to enhance sorption of inorganics from water, *Bioresour. Technol. 246* (2017) 34-47.

Sparks, D.L. (Ed.). (1998). *Soil Physical Chemistry*. 2nd ed., CRC Press, Boca Raton, FL.

State Environmental Protection Administration of China (2002). *Water and Wastewater Monitoring and Analysis Methods,* 4th ed., China Environmental Science Press, Beijing.

Steel, R.G.D., Torrie, J.H., & Dickey, D.A. (1997). *Principles and Procedures of Statistics: A Biometrical Approach,* 3rd ed., McGraw-Hill, New York.

Sun, Y., Gao, B., Yao, Y., Fang, J., Zhang, M., & Zhou, Y. (2014). Effects of feedstock type, production method and pyrolysis temperature on biochar and hydrochar properties, *Chem. Eng. J. 240* (2014) 574-578.

Sun, Y., Iris, K.M., Tsang, D.C., Fan, J., Clark, J.H., & Luo, G. (2020). Tailored design of graphitic biochar for high-efficiency and chemical-free microwave-assisted removal of refractory organic contaminants, *Chem. Eng. J. 398 (2020)* 125505.

Tan, X., Liu, Y., Zeng, G., Wang, X., Hu, X., Gu, Y., & Yang, Z. (2015). Application of biochar for the removal of pollutants from aqueous solutions, *Chemosphere 125* (2015) 70-85.

Thompson, K.A., Shimabuku, K.K., Kearns, J.P., Knappe, D.R.U., Summers, R.S., & Cook, S.M. (2016). Environmental comparison of biochar and activated carbon for tertiary wastewater treatment, *Environ. Sci. Technol. 50 (2016)* 11253-11262.

Tomczyk, A., Sokolowska, Z., & Boguta, P. (2020). Biochar physicochemical properties: Pyrolysis temperature and feedstock kind effects, *Rev. Environ. Sci. Biotechnol. 19 (2020) 191-215.*.

Trakal, L., Bingol, D., Pohorely, M., Hruska, M., & Komarek, M. (2014). Geochemical and spectroscopic investigations of Cd and Pb sorption mechanisms on contrasting biochars, *Bioresour. Technol. 171* (2014) 442-451.

Uchimiya, M., Chang, S., & Klasson, K.T. (2011). Screening biochars for heavy metal retention in soil: Role of oxygen functional groups, *J. Hazard. Mater. 190 (2011)* 432-441.

Valdés, H., Sánchez-Polo, M., Rivera-Utrilla, J., & Zaror, C.A. (2002). Effect of ozone treatment on surface properties of activated carbon, *Langmuir 18* (2002) 2111-2116.

Vikrant, K., Kim, K.H., Ok, Y.S., Tsang, D.C.W., Tsang, Y.F., Giri, B.S., & Singh, R.S. (2018). Engineered/designer biochar for the removal of phosphate in water and wastewater, *Sci. Total Environ. 616--617* (2018) 1242-1260.

Wang, Z., Liu, G., Zheng, H., Li, F., Ngo, H.H., Guo, W., Liu, C., Chen, L., & Xing, B. (2015). Investigating the mechanisms of biochar\'s removal of lead from solution, *Bioresour. Technol. 177* (2015) 308-317.

Wang, J., & Wang, S. (2019). Preparation, modification and environmental application of biochar: A review, *J. Clean. Prod. 227 (2019)* 1002-1022.

Wang, Y., Li, H., & Lin, S. (2022). Advances in the study of heavy metal adsorption from water and soil by modified biochar, *Water 14 (2022)* 3894.

Wang, B., Lan, J., Bo, C., Gong, B., & Ou, J. (2023). Adsorption of heavy metal onto biomass-derived activated carbon, *RSC Adv. 13* (2023) 4275-4302.

Weber, W.J., & Morris, J.C. (1963). Kinetics of adsorption on carbon from solution, *J. Sanit. Eng. Div. 89 (1963) 31-59.*.

World Health Organization (2008). *Guidelines for Drinking-Water Quality: Vol. 1. Recommendations,* 3rd ed., 2nd addendum, World Health Organization, Geneva.

Xiao, X., Chen, B., Chen, Z., Zhu, L., & Schnoor, J.L. (2018). Insight into multiple and multilevel structures of biochars and their potential environmental applications: A critical review, *Environ. Sci. Technol. 52 (2018)* 5027-5047.

Xie, R., Zhu, Y., Zhang, H., Zhang, P., & Han, L. (2021). Effects and mechanism of pyrolysis temperature on physicochemical properties of corn stalk pellet biochar based on combined characterization approach of microcomputed tomography and chemical analysis, *Bioresour. Technol. 329 (2021)* 124907.

Xu, X., Cao, X., Zhao, L., Wang, H., Yu, H., & Gao, B. (2013). Removal of Cu, Zn and Cd from aqueous solutions by the dairy manure-derived biochar, *Environ. Sci. Pollut. Res. 20 (2013)* 358-368.

Xu, D., Zhao, Y., Sun, K., Gao, B., Wang, Z., Jin, J., Zhang, Z., Wang, S., Yan, Y., Liu, X., & Wu, F. (2014). Cadmium adsorption on plant- and manure-derived biochar and biochar-amended sandy soils: Impact of bulk and surface properties, *Chemosphere 111* (2014) 320-326.

Xu, J., Liu, C., Hsu, P.C., Zhao, J., Wu, T., & Tang, J. (2019). Remediation of heavy metal contaminated soil by asymmetrical alternating current electrochemistry, *Nat. Commun. 10 (2019)* 2440.

Xue, Y., Gao, B., Yao, Y., Inyang, M., Zhang, M., Zimmerman, A.R., & Ro, K.S. (2012). Hydrogen peroxide modification enhances the ability of biochar (hydrochar) produced from hydrothermal carbonization of peanut hull to remove aqueous heavy metals, *Chem. Eng. J. 200--202* (2012) 673-680.

Yang, X., Wan, Y., Zheng, Y., He, F., Yu, Z., Huang, J., Wang, H., Ok, Y.S., Jiang, Y., & Gao, B. (2019). Surface functional groups of carbon-based adsorbents and their roles in the removal of heavy metals from aqueous solutions: A critical review, *Chem. Eng. J. 366* (2019) 608-621.

Yao, Y., Gao, B., Chen, J., & Yang, L. (2013). Engineered biochar reclaiming phosphate from aqueous solutions: mechanisms and potential application as a slow-release fertilizer, *Environ. Sci. Technol. 47 (2013)* 8700-8708.

Yuan, X., Xiao, J., & Y, M. (2022). ılmaz, T.C. Zhang, S. Yuan, N, P Co-doped porous biochar derived from cornstalk for high performance CO2 adsorption and electrochemical energy storage, *Sep. Purif. Technol. 299 (2022)* 121719.

Zama, E.F., Zhu, Y.G., Reid, B.J., & Sun, G.X. (2017). The role of biochar properties in influencing the sorption and desorption of Pb(II), Cd(II) and As(III) in aqueous solution, *J. Clean. Prod. 148 (2017)* 127-136.

Zhang, J., Liu, J., & Liu, R. (2015). Effects of pyrolysis temperature and heating time on biochar obtained from the pyrolysis of straw and lignosulfonate, *Bioresour. Technol. 176* (2015) 288-291.

Zhang, X., Zhang, P., Yuan, X., Li, Y., & Han, L. (2020). Effect of pyrolysis temperature and correlation analysis on the yield and physicochemical properties of crop residue biochar, *Bioresour. Technol. 296 (2020)* 122318.

Zhang, Y., Chen, H., & Islam, S. (2025). Advances in biochar modification for environmental remediation with emphasis on iron functionalization, *Biochar X 1 (2025)* e009.

Zhao, L., Cao, X., Masek, O., & Zimmerman, A. (2013). Heterogeneity of biochar properties as a function of feedstock sources and production temperatures, *J. Hazard. Mater. 256--257 (2013)* 1-9.

Zhou, N., Chen, H., Xi, J., Yao, D., Zhou, Z., Tian, Y., & Lu, X. (2017). Biochars with excellent Pb (II) adsorption property produced from fresh and dehydrated banana peels via hydrothermal carbonization, *Bioresour. Technol. 232* (2017) 204-210.

Zhou, L., Richard, C., Ferronato, C., Chovelon, J.M., & Sleiman, M. (2018). Investigating the performance of biomass-derived biochars for the removal of gaseous ozone, adsorbed nitrate and aqueous bisphenol A, *Chem. Eng. J. 334* (2018) 2098-2104.

Zhu, S., Zhao, J., Zhao, N., Yang, X., Chen, C., & Shang, J. (2020). Goethite modified biochar as a multifunctional amendment for cationic Cd(II), anionic As(III), roxarsone and phosphorus in soil and water, *J. Clean. Prod. 247 (2020)* 119579.

## Supplementary Files

This is a list of supplementary files associated with this preprint. Click to download.

- SupplementaryMaterial.docx